Physics-guided deep learning model for daily groundwater table maps estimation using passive surface-wave dispersion

José Cunha Teixeira [1,2], Ludovic Bodet [1], Agnès Rivière [3], Amélie Hallier [2], Alexandrine Gesret [3], Marine Dangeard [2], Amine Dhemaied [2], Joséphine Boisson Gaboriau [2],

[1]Sorbonne Université, CNRS, EPHE, UMR 7619 METIS, 4 place Jussieu, 75252 Paris 05, France
[2]SNCF Réseau, 6 avenue François Mitterrand, 93210 Saint-Denis, France
[3]Geosciences Department, Mines Paris - PSL, PSL University, Paris, France

Key Points:

- Estimating ground water table (GWT) maps from seismic dispersion with deep learning.
- Understanding the spatial and temporal dynamic of the GWT with high resolution.
- Using the GWT geometry and dynamic to constrain the geologic model of the site.

Corresponding author: José Cunha Teixeira, `jose.teixeira@sorbonne-universite.fr`

Abstract

Monitoring groundwater tables (GWTs) is challenging due to limited spatial and temporal observations. This study presents an innovative approach utilizing supervised deep learning, specifically a Multilayer Perceptron (MLP), and continuous passive-Multichannel Analysis of Surface Waves (passive-MASW) for constructing 2D GWT level maps. The study site, geologically well-constrained, features two 20-meter-deep piezometers and a permanent 2D geophone array capturing train-induced surface waves. For each point of the 2D array, dispersion curves (DCs), displaying Rayleigh-wave phase velocities (V_R) across a frequency range of 5 to 50 Hz, have been computed each day between December 2022 and September 2023. In the present study, these DCs are resampled in wavelengths ranging from 4 to 15 m in order to focus the monitoring on the expected GWT levels (between -1 and -5 m). Nine months of daily V_R data around one of the two piezometers is used to train the MLP model. GWT levels are then estimated across the entire geophone array, generating daily 2D GWT maps. Model's performance is tested through cross-validation and comparisons with GWT level data at the second piezometer. Model's efficiency is quantified with the root-mean-square error (RMSE) and the coefficient of determination (R^2). The R^2 is estimated at 80% for data surrounding the training piezometer, and at 68% for data surrounding the test piezometer. Additionally, the RMSE is impressively low at 0.03 m at both piezometers. Results showcase the effectiveness of DL in estimating GWT level maps from passive-MASW data, offering a practical and efficient monitoring solution across broader spatial extents.

Plain Language Summary

This study introduces an innovative method for monitoring groundwater table levels, using a combination of deep learning and passive surface-wave data. The study site, features two piezometers, and a sensor array capturing seismic waves induced by passing trains providing daily seismic wave velocity data, from December 2022 to September 2023. A Multilayer Perceptron model was trained using groundwater table level data from one piezometer and seismic data at the same location. Subsequently, the trained model was applied to estimate groundwater table levels across the entire sensor array area, generating daily maps. The accuracy of the model was tested, revealing an 80% accuracy around the piezometer used in training, and 68% for the other piezometer. Notably, the estimation errors were remarkably low. This research demonstrates the effective use of deep learning in estimating groundwater table levels from passive surface-wave data. It contributes

to the understanding of underground water dynamics, offering a valuable tool for water resource management and environmental hazard monitoring. Importantly, this method allows for efficient groundwater monitoring across large areas using limited data from a single piezometer.

1 Introduction

Groundwater (GW) systems are in dynamic balance between climatic forcing and human pressure. They play a pivotal role in addressing various water resource management and civil engineering matters. Monitoring the dynamics of groundwater table (GWT) geometry is essential for evaluating the resilience and quality of aquifers, predicting water availability, and allowing for sustainable extraction and use, particularly during extreme floods and droughts. Additionally, this understanding proves equally crucial for identifying high-risk infrastructures susceptible to GW-induced natural hazards. In fact, GW floods, landslides (Rahardjo et al., 2010; Panda et al., 2022), and sinkholes (Waltham et al., 2004; Gutiérrez et al., 2014; Parise, 2019; Xiao et al., 2020) are potential threats that can be anticipated and mitigated more effectively by incorporating knowledge of GWT dynamics.

GWTs evolve beneath our feet and still represent a *terra incognita* (Kleinhans, 2005). The assessment of their geometry and dynamics remains a scientific barrier to be lifted. While piezometers can punctually measure GWT levels with high precision and accuracy, it is important to acknowledge that their deployment is often spatially limited, resulting in sparse estimations across larger areas. To reduce this limitation, GWT maps are often interpolated from piezometric data, through techniques such as linear estimators and kriging (Maillot et al., 2019), and represent an important tool for hydrogeologists and civil engineers. While interpolation techniques offer unbiased results for GWT geometry, they do not account for the soil spatial heterogeneity between piezometers and are limited by the spatial distribution and number of piezometers. The effectiveness of the interpolation is contingent on the availability and strategic placement of these monitoring points, impacting the overall accuracy and reliability of the generated GWT maps.

One effective solution to address this limitation involves the conversion of lithofacies into hydrofacies information to constrain GWT map interpolations and simulations (Dagan, 1982; Tsai & Li, 2008). The integration of geophysical data can significantly enhance hydrological knowledge by providing spatial information where conventional hydrological measurement techniques are limited (Dafflon et al., 2009). Time-lapse geophysical methods, offer real-time data on changes in subsurface proprieties, aiding in the characterization of GWT geometry and the identification of spatial variability and temporal trends (Dangeard et al., 2021; Hermans et al., 2023). Methods such as ground-penetrating radar (GPR), induced polarization, self-potential, and resistivity, use the electrical and magnetic properties of the near-surface and are relevant in assessing soil water content (Garambois et al., 2002; Loeffler & Bano, 2004; Samouëlian et al., 2005; Jougnot et al., 2015; Klotzsche et al., 2018). However, they can be ineffective in very electrically conductive or resistive environments. Active seismic approaches, such as seismic reflection, refraction and Multichannel Analysis of Surface Waves (MASW) (Park et al., 1999) have been successfully used for water content monitoring (Lu, 2014; Bergamo et al., 2016) and 1D GWT geometry characterization (Pasquet et al., 2015a, 2015b; Dangeard et al., 2021). They mostly rely one the study of the pressure-(P) and shear-(S) wave velocities (V_P and V_S) to estimate V_P/V_S or Poisson's ratios (Biot, 1956a, 1956b), which are sensitive indicators of fluid presence. However they face limitations due to the difficulty to regularly deploy active sources in adverse conditions, making continuous characterizations impossible.

Passive seismic methods, use continuous and coherent ambient seismic noise generated by natural or anthropogenic activities. They rely on seismic interferometry and consist in the Green's function retrieval by cross-correlation between recording sensors pairs to provide a characterization of the propagation medium (Aki, 1957; Derode et al., 2003; Weaver & Lobkis, 2004; Wapenaar, 2004; Wapenaar et al., 2010a, 2010b; Larose et al., 2015). Some approaches monitor the relative temporal variation of seismic velocities (dv/v) for specific wavefronts between pairs of sensors, and have put on evidence a clear correlation with GWT level variations (Grêt et al., 2006; Voisin et al., 2016; Lecocq et al., 2017; Voisin et al., 2017; Clements & Denolle, 2018; Garambois et al., 2019; Kim & Lekic, 2019; Barajas et al., 2021; Mao et al., 2022; Qin et al., 2022; Zhang et al., 2023). Although these methods are able to generate 2D GWT variation maps, as recently shown by Gaubert-Bastide et al. (2022), they provide limited information about the aquifer geometry and the proper GWT levels.

Another employed approach is the passive-MASW, an extension of the standard active-MASW. This technique relies on the propagation of ambient Rayleigh-waves, induced by cars or trains, through linear geophone arrays to characterize the near-surface and has found application in various civil engineering contexts, both sporadically in time with 1D setups (Park & Miller, 2008; Quiros et al., 2016; Cheng et al., 2015, 2016; Mi et al., 2022; Czarny et al., 2023; Rezaeifar et al., 2023; You et al., 2023; Mi et al., 2023; Cunha Teixeira et al., submitted), and for continuous sinkhole monitoring with 2D configurations (Bardaine & Rondeleux, 2018; Bardainne et al., 2022; Tarnus et al., 2022a, 2022b; Bardainne et al., 2023). The characterization process is based on the analysis of dispersion curves (DCs), which depict the fluctuation of Rayleigh-wave phase velocity (V_R) across frequencies, along the linear arrays. V_R variation over frequency, seen in DCs, is closely linked to the medium's V_S variation over depth, which, is influenced by the water content (Solazzi et al., 2021). Nevertheless, the shift from dispersion curves (DCs) to ground models incorporating water saturation profiles and GWT level information involves intricate inversion operations, combining geophysical and hydrogeological data, that are still under development (Sanchez Gonzalez et al., in prep).

Piezometers offer valuable but localized and sparse hydrogeological data, while geophysical methods help in interpolating and extrapolating this information. However, geophysical methods often lack direct connections to hydrogeological principles. More recently, machine learning (ML) and deep learning (DL) methodologies have gained significant prominence in hydrology and water resource applications (see Tripathy and Mishra (2024) for an overview on DL usage in hydrology). More specifically, physics-guided models, incorporating geophysical knowledge into ML or DL models, can effectively handle and uncover hidden patterns in complex and high-dimensional datasets, and serve as a bridge between hydrogeology and geophysics. Abi Nader et al. (2023) combined ML and seismic monitoring to appraise punctual GWT levels with great precision, using raw seismic noise records. Cai et al. (2022) was able to estimate GWT levels with more accuracy with a physics-guided DL model than with a pure DL model, using water balance equations as a physical constraint.

This study takes advantage of a geologically well constrained sinkhole-affected site equipped with a dense geophone array and two piezometers. It offers almost a year of observed passive seismic data, revealing temporal tends that could be correlated with the GWT level seasonal variations. The objective of this study is to demonstrate the utility of DCs, obtained through passive seismic methods, in monitoring GWT levels. We introduce an innovative physics-guided DL method, coupling 2D passive-MASW and a MLP, to estimate daily 2D GWT maps from a single piezometer. After introducing the test site and providing a comprehensive overview of the passive-MASW survey geometry and data, we give a description of the method employed for building, training and testing the MLP. Subsequently, we showcase the generated 2D GWT maps resulting from the application of this method, discuss the hydrogeological implications, and explore the limitations associated with such approach.

2 Study site and data

2.1 A sensitive but well constraint site

The study site is located along a railway line in the Grand-Est region of France (see Figure 1a,b) at the eastern edge of the Paris Basin. The site area has a stratigraphic composition characterized by an 80-meter-thick cover formation, primarily composed of middle and lower Muschelkalk alluvium, clays, and marls originating from the middle Triassic period, underlayed by a substratum layer of lower Triassic sandstones (LTS). The hydrological context of this cover layer has not been studied at the local scale of the site. Only a large GWT map of the LTS aquifer from 2010 is available at the Lorraine region scale (Nguyen-Thé et al., 2010). At the acknowledgment of the authors, the connectivity of the cover layer alluvium aquifer with the LTS aquifer is not determined, and will not be discussed.

Between 1989 and 2017, this railway site has encountered several instances of sinkhole dropouts, particularly impacting the integrity of the railway on the southwest side towards the bridge (see Figure 1b). These sinkholes are attributed to gypsum dissolution in the marl layers. Consequently, a cement-based grout was injected at a depth of 20 m in the soil to reinforce the structure in 2018. Five Auger drilling tests with depths up to 20 m were conducted in December 2022 with the aim of detecting potential eventual cavities, as depicted in Figure 1b. These tests revealed no cavities and facilitated a visual characterization of the various layers constituting the near-surface (see Figure 1c). An approximately 10 m-thick layer of alluvium, consisting of a mixture of sand and clay, appears to overlay a denser layer of marly clays and highly compact marls. This observation aligns coherently with the expected geological composition of the middle and lower Muschelkalk layer.

2.2 Monitoring setup and data

To effectively address and mitigate the risks posed by sinkholes, a continuous ground monitoring through 2D passive-MASW using seismic noise induced by trains (Bardaine & Rondeleux, 2018; Bardainne et al., 2022; Tarnus et al., 2022a, 2022b; Bardainne et al., 2023), combined with two piezometers has been established as the best approach in late

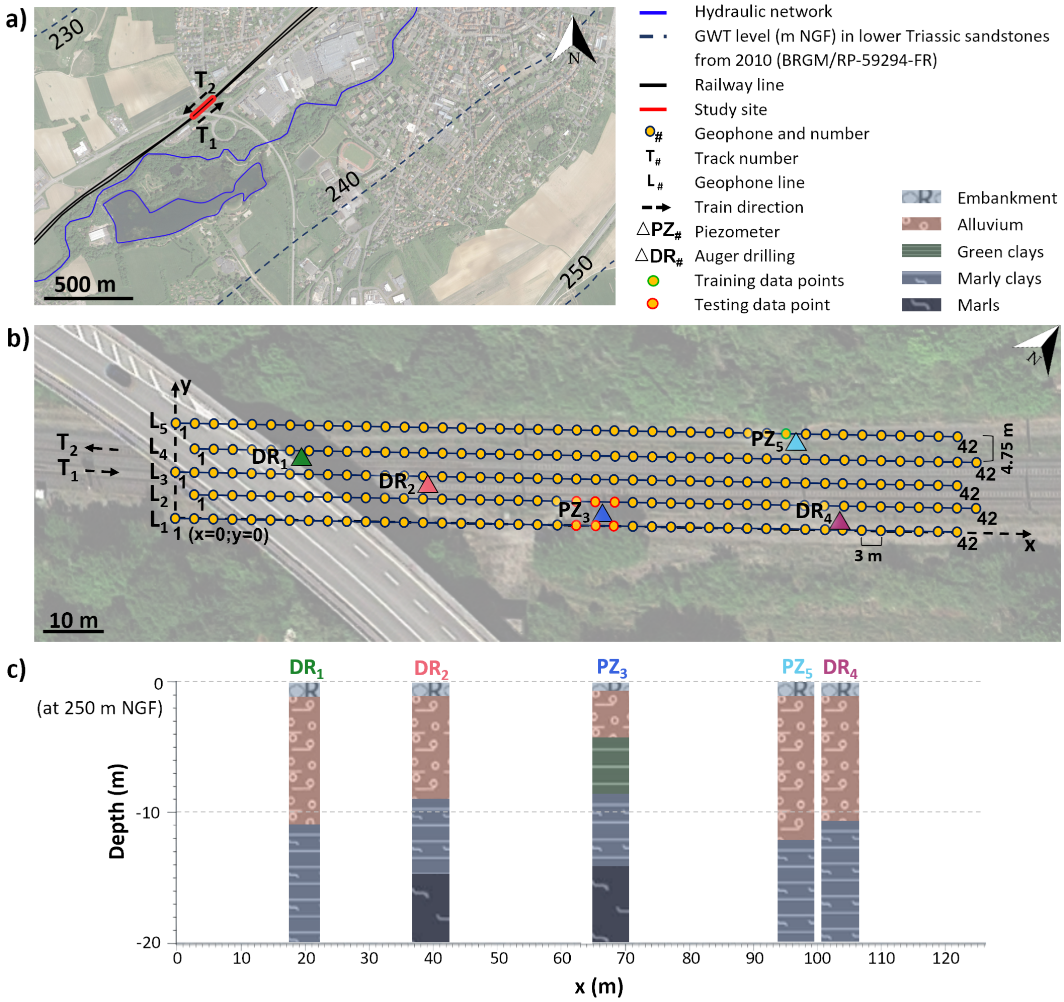

Figure 1. (a) Location map of the site with hydraulic networks and GWT levels of the lower Triassic sandstone aquifer. (b) Experimental design of the study site showing the five lines (L_1 to L_2) of 42 geophones (yellow dots), planted parallel to the railway tracks, and the track numbers (T_1 and T_2) with train directions. x and y correspond to the distance parallel and perpendicular to the railway tracks, respectively, and point ($x = 0; y = 0$) is at geophone 1 of array line 1 ($L_1 - P_1$). Data points used for training and testing the MLP are colored in red around piezometer PZ_3, and green close to piezometer PZ_5, respectively. DR_1, DR_2, and DR_4 correspond to Auger drilling locations without piezometers. (c) Lithographic log at the 5 drillings. The lithology consists of an alluvial layer of sand and clay that is roughly 10 meters thick, overlying a denser section of marly clays and highly compact marls.

2020. Following the installation of the piezometers in late 2022, the studied period extends from December 30, 2022, to September 3, 2023.

Passive seismic noise induced by train passages has been recorded using five uniform linear arrays (L_1 to L_5 on Figure 1b), since September 2020. Each linear array has a length of 123 m and is equipped with 42 3-meter spaced geophones. The geophones were strategically positioned along the rail track, either on the cess (i.e., the track side) for linear arrays L_1 and L_5, or on the ballast for L_2, L_3, and L_4. Daily DCs have been estimated at each point of the array , covering a frequency range from 5 to 50 Hz., and resampled in wavelengths ($\lambda = V_R/f$) within the range of 4 to 15 m, with a step of 0.5 m.

V_R variation over frequencies or wavelengths, seen in DCs, is linked to the medium's shear velocity (V_S) variation over depth. However, it's crucial to note that this transformation is nonlinear. Yet, wavelength resampling offers a more accurate link to depth in comparison to frequencies, enabling precise targeting of the first meters of the near-surface. Typically, the depth is around half or one-third of the wavelength (Shtivelman, 1999; Foti et al., 2018). Therefore, this resampling should primarily target depths ranging from -1.5 to -5 m.

Figure 2 shows every estimated daily DC, from December 30, 2022, to September 3, 2023, sampled over frequencies and wavelengths, close to PZ_3 at point 23 of geophone line 1 (L_1-P_{23}), and close to PZ_5 at point 33 of geophone line 5 (L_5-P_{33}) (see Figure 1b). In Figure 3, examples of V_R pseudo-sections showcase the DCs sampled over wavelengths along the 5 linear arrays, on April 1, 2023, and July 1, 2023, at high and low water periods, respectively (see Figures 4a,b). V_R pseudo-sections over frequencies version is shown in Figure A1 of Appendix A. Figures 2 and 3 reveal a spatial and temporal evolution of V_R that could be correlated with GWT geometry and dynamics. This indicates the potential utility of employing this method for the ongoing monitoring purposes.

Both piezometers were equipped on December 30, 2022, at two of the five drilling locations, and have been recording daily GWT levels over time (see PZ_3 and PZ_5 in Figure 1b). GWT level data at PZ_3 and PZ_5 is presented in Figures 4a and b. Both GWT levels are situated within the alluvium layer (see Figure 1c). However, the two piezometers display distinct behaviors. PZ_3 is more responsive, and displays greater amplitude variations, in comparison with PZ_5. Figures 4c and d show V_R variation over time for all wavelengths at both piezometer locations. It's worth noting that the steep change in V_R at $\lambda = 8$ m observed in Figures 2c and 4c could correspond to the GWT level at PZ_4. However, conclusive determination requires inversion of the DCs into V_S over depth models. Overall, despite the differences in shape between DCs at the two piezometers (see Figures 2c and d), there seems to be a correspondence with the observed trends in GWT level variations at array points close to each piezometer. When GWT level decreases, there is a corresponding increase in V_R, and conversely, when GWT level rises, V_R tends to decrease. The anti-correlated variation is evident across all wavelengths at different scales, as depicted in Figures 4c and d, and becomes even more pronounced when focusing on specific wavelengths in Figures 4e and f. This inverse relationship between GWT levels and V_R is indicative of the influence of groundwater dynamics on the spatial distribution and temporal evolution of V_R. Indeed, if DCs demonstrate such anti-correlation with GWTs levels at these locations, then it is reasonable to expect that this anti-correlation extends to every point along the seismic array. We propose training a DL model using seismic and GWT level data from PZ_3, as it exhibits the most pronounced responsiveness among the two piezometers. The goal is to be able to translate DCs into GWT levels, and subsequently estimate GWT levels at the remaining points along the entire array.

3 Method

3.1 Multilayer Perceptron architecture

In this study, a MLP is used as a regression tool for estimating a GWT level from a single DC, at several seismic array points and times. The MLP is the most basic feed-forward artificial neural network and consists of multiple layers of fully connected neurons, comprising an input layer, one or more hidden layers, and an output layer (Rosenblatt, 1958; Murtagh, 1991). The use of a MLP allows for complex non-linear mappings between inputs and outputs, making it particularly well-suited for capturing intricate relationships within datasets.

A MLP with two hidden layers and $k = 32$ neurons per layer was used in this application (see Figure 5). The input and output layer sizes correspond to the number of features of the input and output data. For each estimation, an unique DC of V_R resampled over wavelengths ranging from 4 to 15 m and with a wavelength step of 0.5 m, is used as input, which can be seen a vector $\boldsymbol{x}$ of size $n = 23$. The output corresponds to an unique scalar

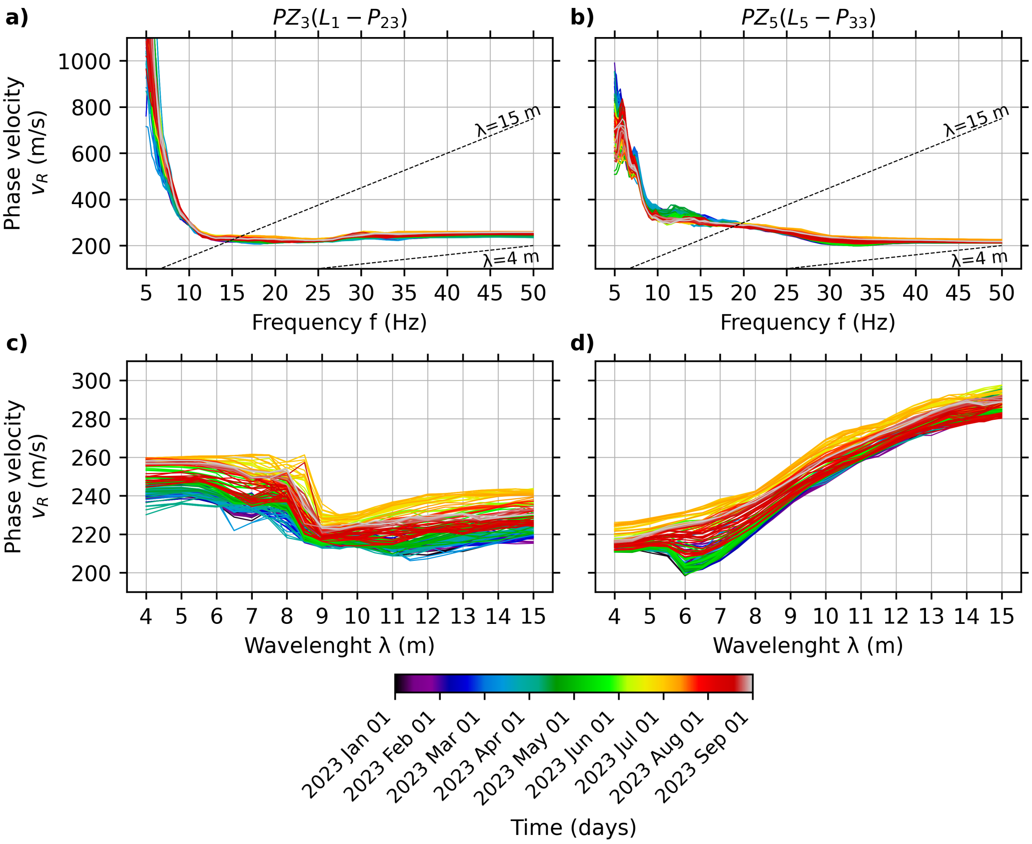

Figure 2. Time-series of raw dispersion curves over frequencies obtained (a) at seismic array point L_1-P_{23}, close to piezometer PZ_3, and (b) at seismic array point L_5-P_{33}, close to piezometer PZ_5. Resampled dispersion curves over wavelengths, ranging from $\lambda = 4$ to $\lambda = 15$ m, (c) at seismic array point L_1-P_{23}, close to piezometer PZ_3, and (d) at seismic array point L_5-P_{33}, close to piezometer PZ_5 (see Figure 1b).

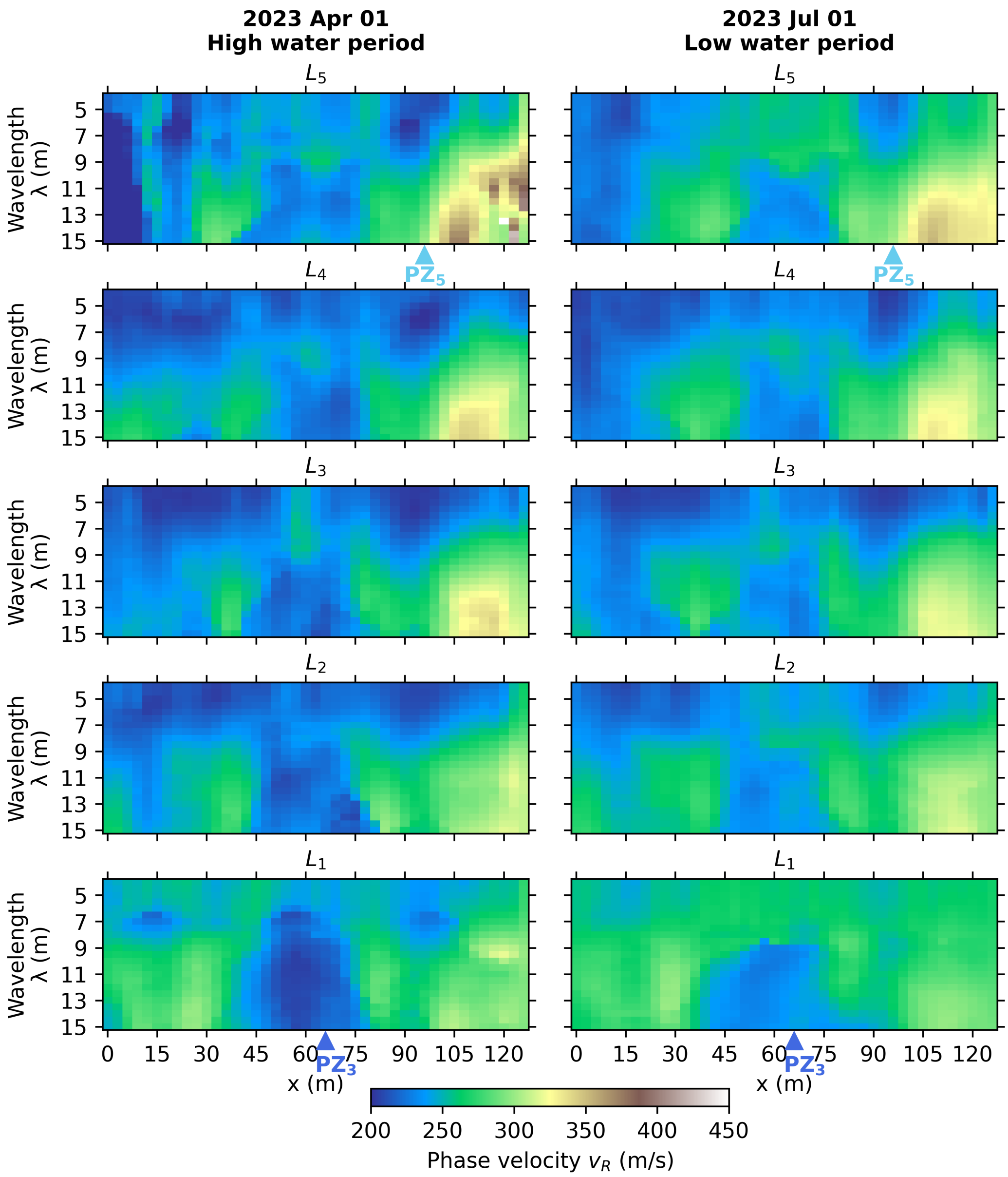

Figure 3. V_R pseudo-sections over wavelengths for the 5 linear geophone arrays (L_1 to L_5) (left) at a high water period on April 1, 2023, and (right) at a low water period on July 1, 2023. Positions of piezometers PZ_3 and PZ_5 are represented by the blue triangles on pseudo-sections L_1 and L_5, respectively.

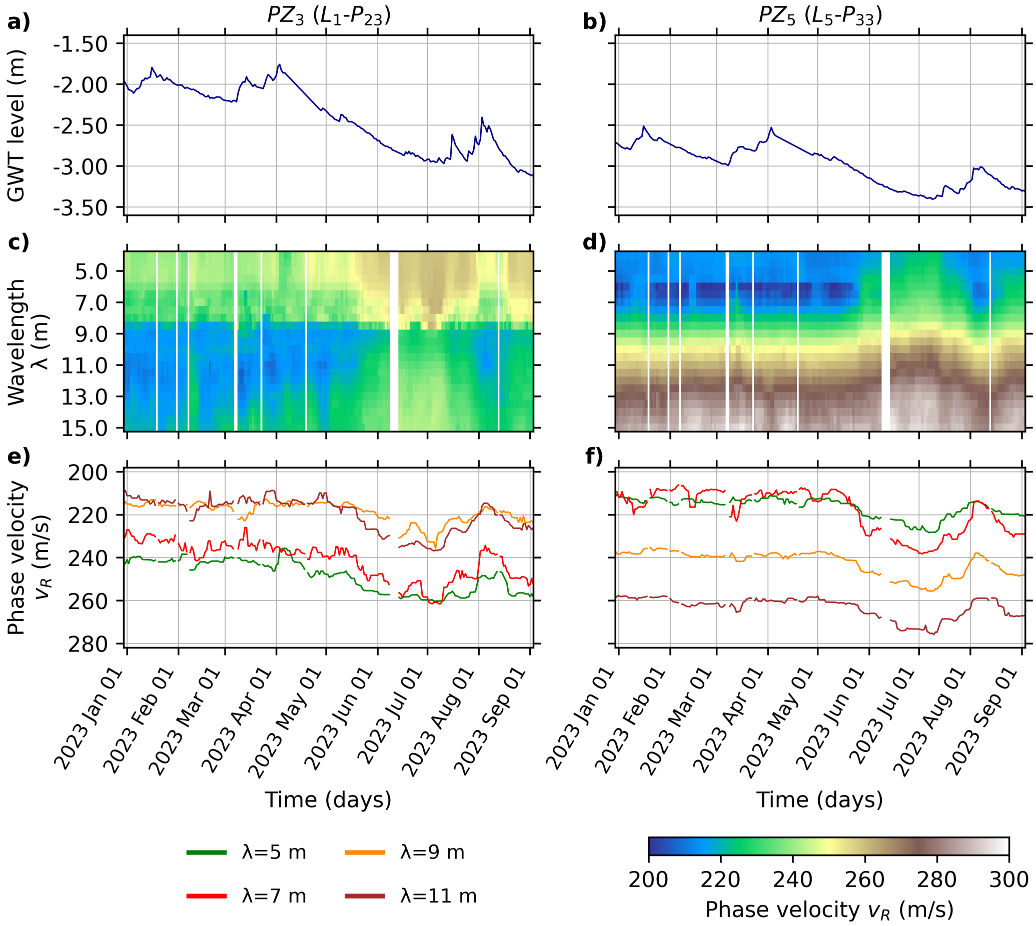

Figure 4. (a) and (b) Recorded GWT levels between December 30, 2022, and September 3, 2023, at PZ_3 and PZ_5. (c) and (d) V_R over wavelengths evolution over the same time period at seismic array points L_1-P_{23}, close to PZ_3, and L_5-P_{33}, close to PZ_5. (e) and (f) V_R at wavelengths 5, 7, 9, and 11 m evolution over the same time period at seismic array points L_1-P_{23}, close to PZ_3, and L_5-P_{33}, close to PZ_5.

y of an estimated GWT level. For each layer l, let $\boldsymbol{w}^{(l)}$ be a vector of weights, initially containing arbitrary values, and $\boldsymbol{b}^{(l)}$ a vector of constants called "bias".

At the first layer $l = 1$, the perceptron calculates

$$z_j^{(1)} = b_j^{(1)} + \sum_{i=1}^{n} w_{ij}^{(1)} x_i \ , \tag{1}$$

for each neuron j over the k neurons of the first hidden layer, and with each feature i over the n features of the input vector $\boldsymbol{x}$. Then, the vector $\boldsymbol{z}^{(1)}$ goes through a *Rectified Linear Unit* function $ReLu$ introducing non-linearity to the model:

$$h_j^{(1)} = ReLu(z_j^{(1)}) = \begin{cases} z_j^{(1)} & \text{if } z_j^{(1)} > 0, \\ 0 & \text{otherwise.} \end{cases} \tag{2}$$

At the second layer $l = 2$, the perceptron calculates

$$z_j^{(2)} = b_j^{(2)} + \sum_{i=1}^{k} w_{ij}^{(2)} h_i^{(1)} \ , \tag{3}$$

for each neuron j over the k neurons of the second layer, and with each neuron i over the k neurons of the previous first hidden layer. Again, the vector $\boldsymbol{z}^{(2)}$ goes through a *Rectified Linear Unit* function $ReLu$:

$$h_j^{(2)} = ReLu(z_j^{(2)}) = \begin{cases} z_j^{(2)} & \text{if } z_j^{(2)} > 0, \\ 0 & \text{otherwise.} \end{cases} \tag{4}$$

Finally, at the output layer, the perceptron calculates

$$z_1^{(out)} = b_1^{(out)} + \sum_{i=1}^{k} w_{i1}^{(out)} h_i^{(2)} \ , \tag{5}$$

for the unique neuron of the output layer, and with each neuron i over the k neurons of the previous second hidden layer. Finally, $z^{(out)}$ goes through an *Identity* activation function *linear*, which is the equivalent of no activation, to obtain the estimated scalar value y:

$$y = linear(z^{(out)}) = z^{(out)} \ . \tag{6}$$

3.2 Data preprocessing and training

The MLP goes through a training phase to optimize its performance and enhance its ability to make accurate estimations. The training data involved daily DCs measurements at specific seismic array points surrounding PZ_3 (L_1-P_{22}, L_1-P_{23}, L_1-P_{24}, L_2-P_{21}, L_2-P_{22}, and L_2-P_{23}) as inputs, and daily GWT level measurements at PZ_3 as expected outputs.

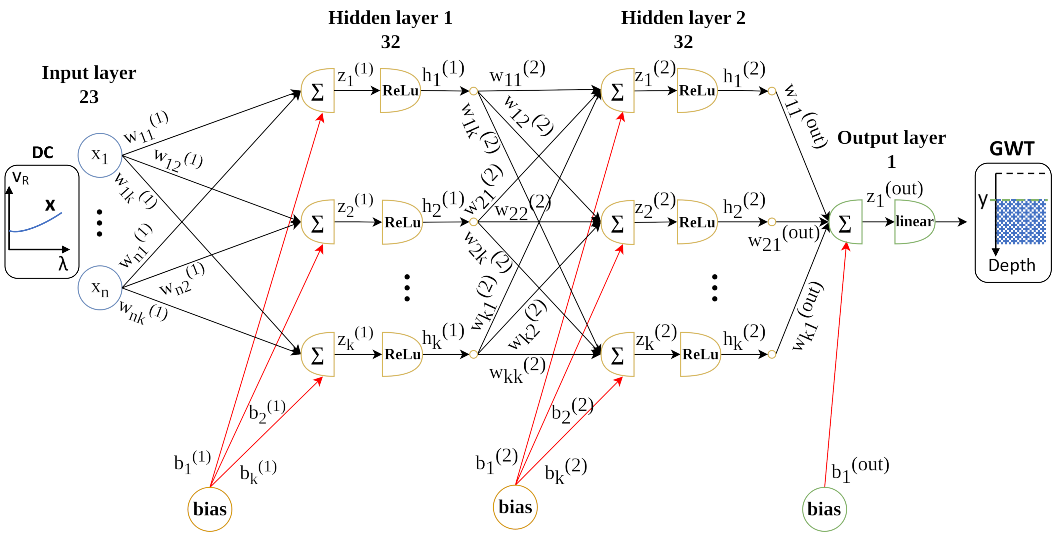

Figure 5. Multilayer perceptron with an input layer, two hidden layers, and an output layer. A DC (V_R over wavelength λ) is used as input to predict a GWT level. The input vector $\boldsymbol{x}$ has $n = 23$ features, each hidden layer l has $k = 32$ neurons, and the output y is a scalar. $\boldsymbol{w}^{(l)}$ is a weight or leaning coefficient vector and $\boldsymbol{b}^{(l)}$ a vector of constants called "bias". *ReLu* and *linear* are the *Rectified Linear Unit* and *Identity* activation functions.

Thus, for an unique day and a unique GTW level output, six different inputs are used, corresponding to the closest six points around the piezometer. Due to the similarity of the DCs at these points, this allows for a better spatial versatility of the model, and can be seen as data augmentation (Shorten & Khoshgoftaar, 2019). To facilitate the training phase, DCs were normalized by 2000 (i.e., around twice the maximum observed V_R) and GWT levels were used in absolute numbers. This data collection spanned from December 30, 2022, to September 3, 2023, encompassing a total of 248 days. Days without data due to technical issues were excluded from the dataset.

During the training process, weights and biases are refined to minimize the difference between estimated outputs and actual target values. The training begins with the presentation of training data, with known input and outputs, to the MLP. Subsequently, the calculated errors in terms of *root-mean-square error* (RMSE) of the resulting estimations are backpropagated through the network (Rosenblatt, 1958; Linnainmaa, 1976; Werbos, 1982). This involves adjusting the weights and biases in the opposite direction of the error gradient. In this study, the magnitude of these adjustments was determined by a stochastic gradient descent *Adam* optimization algorithm with a learning rate of 10^{-4}, which fine-tunes the model iteratively (Kingma & Ba, 2014). This iterative adjustment process was done until the MLP converges to a state where further refinement did not significantly improve its estimation capabilities. The desired outcome was a trained MLP with optimized internal parameters enabling it to generalize well to new, unseen data, making accurate estimations in various scenarios.

A maximum of 1000 training epochs (i.e., iterations) with 2 samples per gradient update were done. Daily DCs measurements at seismic array points surrounding PZ_5 (L_4-P_{31}, L_4-P_{32}, L_4-P_{33}, L_5-P_{32}, L_5-P_{33}, and L_5-P_{34}), and GWT levels at PZ_5 were used as a validation dataset for "early-stopping", to limit the number of epochs and avoid model overfitting (Ying, 2019; Tripathy & Mishra, 2024).

4 Results

Figure 6 compares the GWT levels observed at PZ_3 and PZ_5 with the estimations at seismic array points L_1-P_{23} close to PZ_3, and L_5-P_{33} close to PZ_5, between December 30, 2022, and September 3, 2023. As anticipated, the estimated and observed values for PZ_3, which was used in the training process, show a close proximity (see Figures 6a and b), with an RMSE of 0.03 m and a *coefficient of determination* R^2 of 80 % (see Appendix D for definitions). Please note that this score could possibly be higher but is limited to able a great generalization of the model. While the model successfully captures the general patterns, it exhibits minor fluctuations that deviate from the observed values. Despite these slight deviations, the overall agreement between estimated and observed values underscores the model's capability to replicate the general trends associated with PZ_3. The model also demonstrates its ability to accurately extrapolate and estimate GWT levels at PZ_5, a location not included in the training set (see Figures 6c and d). Estimations for PZ_5 yield a RMSE of 0.03 m and a R^2 of 68%, suggesting a low level of estimation error and a high degree of accuracy. However, GWT levels are slightly overestimated by 25 cm between May and June 2023 and between August and September 2023. These errors could certainly be corrected by extending the time span of groundwater table (GWT) level data used for training, a limitation imposed by the time-frame of this research.

Figures 7b-i show 2D GWT maps with estimations made at each seismic array point, at the beginning of January, February, April, May, June, July, August, and September, 2023. Estimated GWT levels at the five drilling locations, are highlighted in Figure 7a.

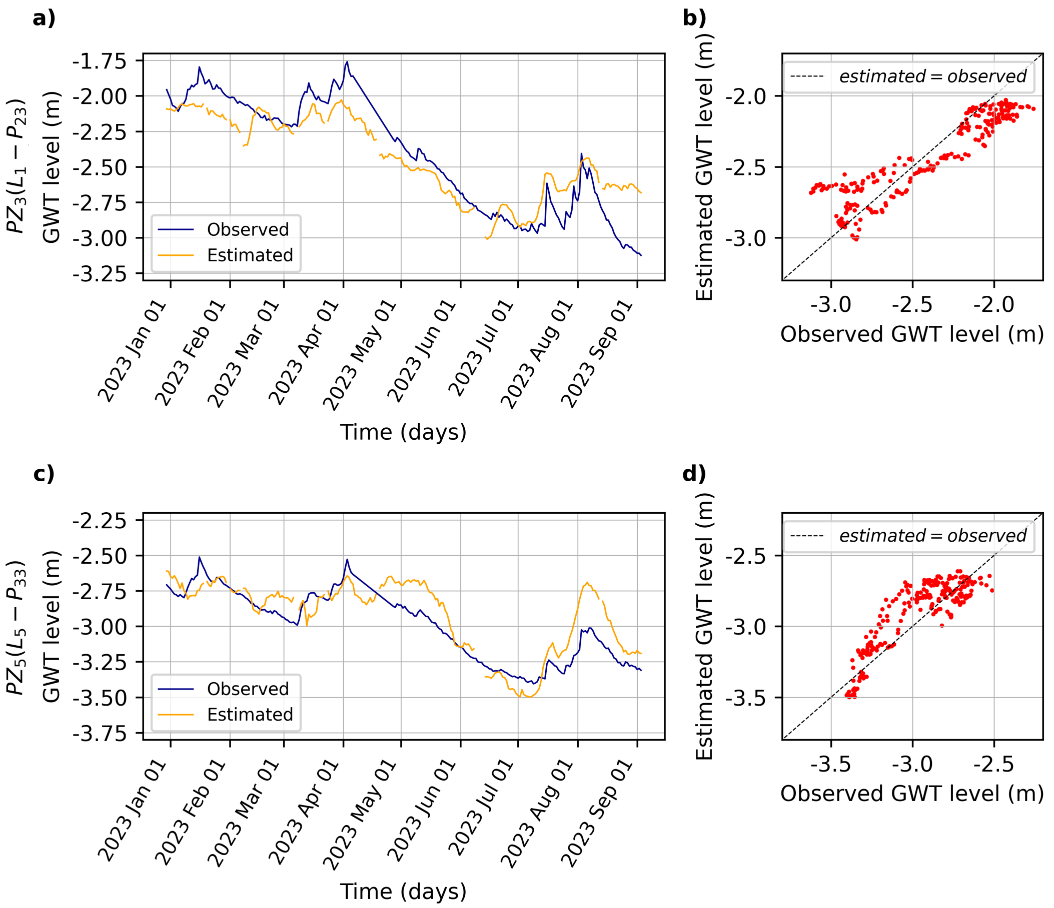

Figure 6. MLP's GWT level estimations, obtained using DCs at seismic array points around PZ_3 (L_1-P_{22}, L_1-P_{23}, L_1-P_{24}, L_2-P_{21}, L_2-P_{22}, and L_2-P_{23}) and observed GWT levels at PZ_3 as training data. (a) GWT level over time observed at PZ_3 and estimated at seismic array point L_1-P_{23}. (b) GWT levels observed at PZ_3 versus estimated at L_1-P_{23}. (c) GWT level over time observed at PZ_5 and estimated at seismic array point L_5-P_{33}. (d) GWT levels observed at PZ_5 versus estimated at point L_5-P_{33}.

The GWT maps exhibit a noticeable global variation, approximately 1 m, between the high water period (April 2023) and the low water period (July 2023) (see Figure 8). Nevertheless, a spatial heterogeneity over x and y is evident, revealing zones with relatively both high and low GWT levels. More specifically, the area between $x = 0$ and $x = 20$ m, comprising DR_1 and DR_2, consistently exhibits elevated levels at around -2 m, with minimal variation over time. This region corresponds to the 20-meter deep grout-injected zone. The area between $x = 30$ and $x = 60$ m, encompassing PZ_3, and between $x = 80$ and $x = 90$ m, encompassing $PZ5$, demonstrate elevated levels from January to May 2023. However, a noticeable decline is observed during the summer months. In the central area of the map, a small low-level zone with minimal variation over time, enclosed by a high-level zone, can be noticed. Regions between $x = 20$ and $x = 30$ m, and between $x = 60$ and $x = 80$ m, exhibit relatively low GWT levels. Additionally, the zone between $x = 90$ and $x = 126$ m, which includes DR_4, displays the lowest GWT levels. For reference, this zone also registered the highest values of V_R (see Figure 2). Artifacts exhibiting very high GWT level estimations (between 0 and -1 m) and very low GWT level estimations (around -6 m) can be observed at the border of the maps, along geophone line L_5, between February and May 2023 (see Figures 7c,d,e). These artifacts are also observed in the raw V_R input data and were likely initially induced during the computation and picking of the DCs.

5 Discussion

5.1 Geologic interpretation

Spatial and temporal variations in GWT levels observed in Figures 7 and 8 could be explained by differences in lithology over the studied site, effectively captured by seismic data. Areas with elevated GWT levels may be attributed to the presence of highly impermeable materials below alluvium, such as grout or clay. In such case, GW is impeded from infiltrating into the subsurface, contributing to the observed elevated GWT levels. Areas exhibiting consistently high GWT levels with minimal variation could be attributed to the presence of shallow, highly impermeable materials, such as clay, beneath the alluvium layer. Areas with high GWT levels during high-water periods, and low GWT levels during low-water periods, could be attributed to the presence of a deeper highly impermeable material beneath alluvium. Conversely, areas with constant low GWT levels may be associated with more permeable materials beneath alluvium. Figure 9 shows the GWT cross-section traversing through all five drilling points, for different months along the year, accompanied

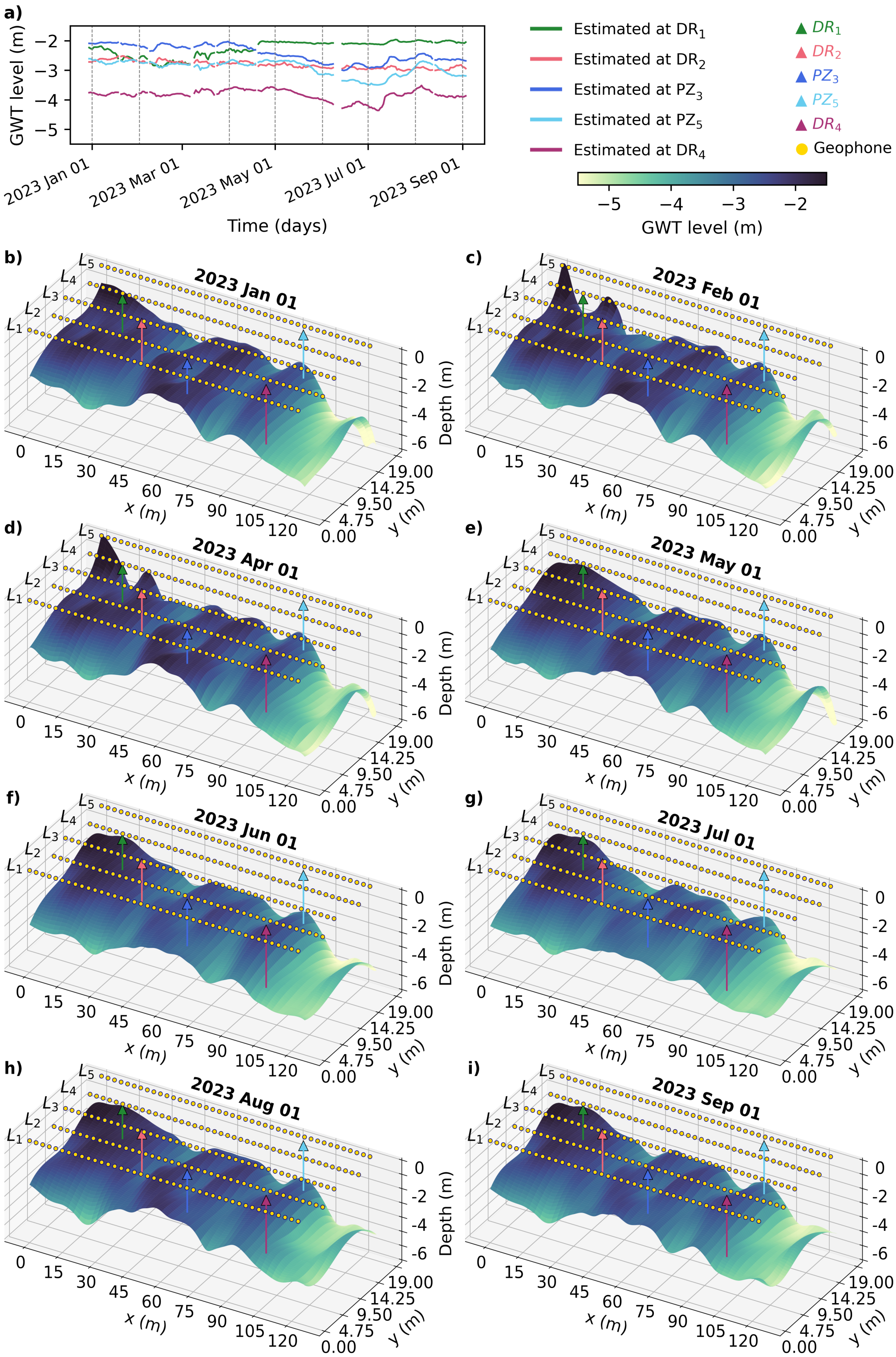

Figure 7. MLP's GWT level estimations, obtained using DCs at seismic array points around PZ_3 (L_1-P_{22}, L_1-P_{23}, L_1-P_{24}, L_2-P_{21}, L_2-P_{22}, and L_2-P_{23}) and observed GWT levels at PZ_3 as training data. (a) Estimated GWT levels over time at the five drilling and piezometers locations. (b) to (i) Estimated GWT level 2D maps at different dates, with geophone linear array ($L_{\#}$), piezometer ($PZ_{\#}$) and drilling ($DR_{\#}$) positions at the surface.

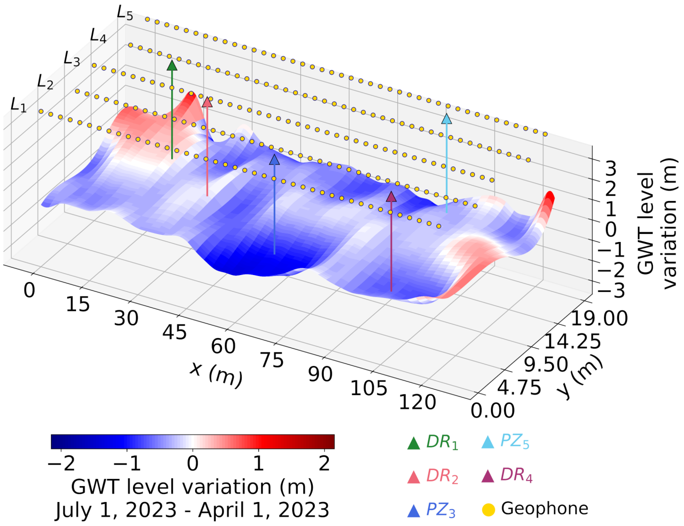

Figure 8. Estimated GWT level 2D map variation between high water period (April 1, 2023) and low water period (July 1, 2023), obtained using DCs at seismic array points around PZ_3 (L_1-P_{22}, L_1-P_{23}, L_1-P_{24}, L_2-P_{21}, L_2-P_{22}, and L_2-P_{23}) and observed GWT levels at PZ_3 as training data. Geophone, piezometer and drilling positions are displayed at surface.

by geological logs illustrating the nature of the materials encountered. As expected, the GWT is higher with greater variation above the shallow clay layer (drilling at PZ_3). Between DR_2 and PZ_3, close to DR_2, as well as between PZ_3 and PZ_5, there is a decrease in the GWT, with a distinctive pinching point. This could be explained by a transition from highly impermeable to more permeable materials. All this suggests that zones $x = 30$ and $x = 60$ m, and between $x = 80$ and $x = 90$ m in a lesser degree, present a shallow clay layer.

5.2 Model robustness

Pseudo-sections of V_R over wavelengths for the five geophone array lines, computed during the high water period (April 1, 2023) and the low water period (June 1, 2023), and displayed in Figure 2, were inverted into sections of V_S over depth (see Figure 10 and Figure C1 in Appendix C). Remarkably, on the five sections, the estimated GWT levels align perfectly with a low-velocity layer (blue on Figure 10) characterized by a V_S between 200 and 250 m/s during these two periods. This alignment supports the credibility of the method, as the MLP successfully estimated the depth of this layer despite the absence of direct depth information in DCs. It is noteworthy that the GWT is closer to the surface where this low-velocity layer is shallower and exhibits lower V_S values. Around $x = 60$

on L_1, this low-velocity layer is placed just above the observed clay layer at drilling point PZ_3. This observation strongly supports the hypothesis that the low-velocity layer might be associated with saturated alluvium, and that its depth is influenced by the presence of an underlying clay layer. Conversely, zones with higher V_S also show lower GWT levels that seem to follow deep low-velocity layer, implying deeper saturated alluvium. This aligns with the absence of clay observed in the drillings and indicating a deeper interface between alluvium and the impermeable underlying marl layer.

To assess the influence of the number of piezometers on the estimated GWT level maps, a model was trained using data points around PZ_3 (L_1-P_{22}, L_1-P_{23}, L_1-P_{24}, L_2-P_{21}, L_2-P_{22} and L_2-P_{23}) and PZ_5 (L_4-P_{31}, L_4-P_{32}, L_4-P_{33}, L_5-P_{32}, L_5-P_{33} and L_5-P_{34}). The results, presented in Appendix B (see Figures B1, B2, B3, B4, and B5), reveal an enhanced estimation performance at both PZ_3 (R^2 of 88% and an RMSE of 0.01 m) and PZ_5 (R^2 of 72% and an RMSE of 0.01 m). Upon comparing the estimated GWT maps in Figures 7 (MLP trained with only PZ_3) and B2 (MLP trained with both PZ_3 and PZ_5), it is evident that extreme high and low GWT level values appear to have been smoothed or flattened. Nevertheless, the general GWT levels and behavior remain highly consistent with the previous estimations. This supports the robustness of using an unique piezometer for training. However, employing multiple piezometers for different lithologies enhances the precision and stability of the method.

6 Conclusions

This study introduces a physics-guided DL model, combining 2D passive-MASW with a MLP, that estimates daily 2D GWT maps from a single piezometer. This hybrid approach offers an effective mean of monitoring GWTs with both spatial and temporal precision. The method exhibits notable generalization capabilities, with the ability to spatially extrapolate GWT level maps beyond the training dataset. Analysis of GWT maps reveals spatial and temporal variations, offering a nuanced understanding of GWT geometry and dynamics, and revealing valuable hydrogeological insights. The model successfully captures variations associated with lithological changes, demonstrating its efficacy in characterizing subsurface materials. In addition, the estimated GWT levels align closely with low-velocity layers, in terms of V_S, indicative of saturated alluvium and shallow clay layers. However, while the study demonstrates promising results, it is crucial to acknowledge its limitations. The model's performance may be influenced by site-specific conditions, and further validation

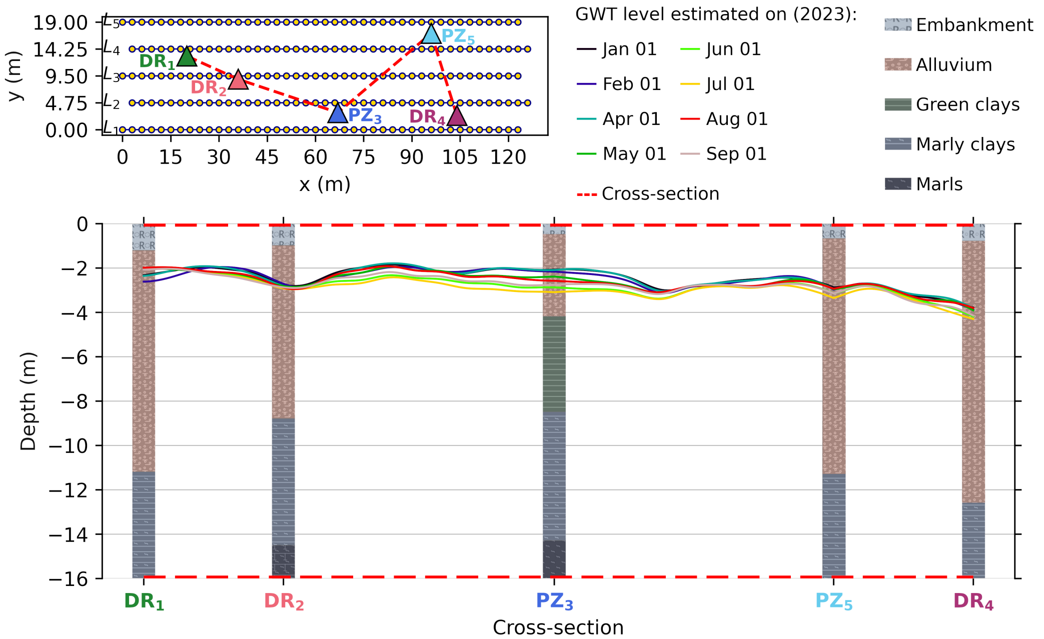

Figure 9. (a) Geophone array map and cross-section line (in red) between drilling and piezometers. (b) Cross-section of estimated GWT levels at different dates, obtained using DCs at seismic array points around PZ_3 (L_1-P_{22}, L_1-P_{23}, L_1-P_{24}, L_2-P_{21}, L_2-P_{22}, and L_2-P_{23}) and observed GWT levels at PZ_3 as training data, with geologic logs illustrating the nature of the underground materials.

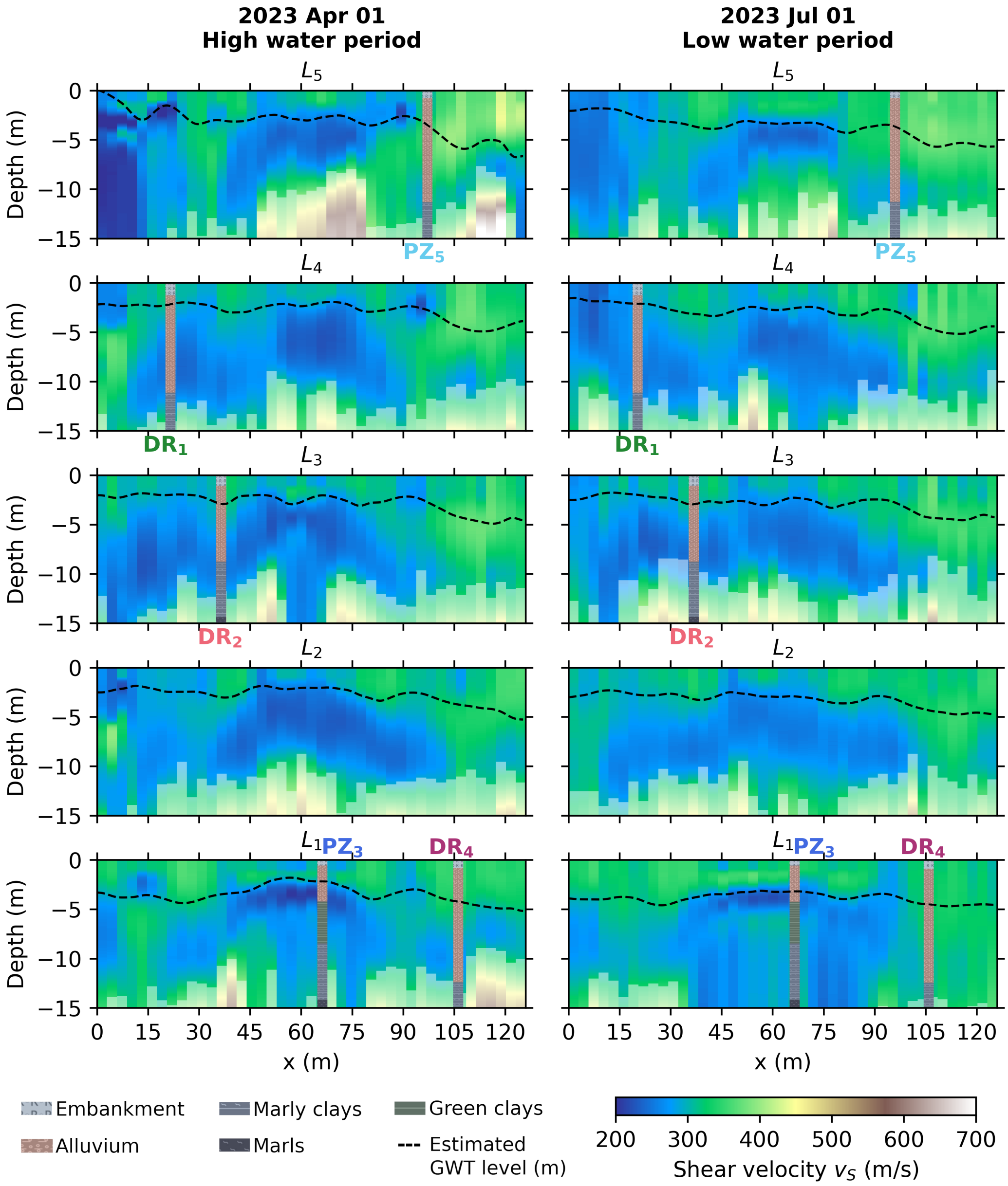

Figure 10. Inverted V_S sections over depth for the 5 linear geophone arrays (L_1 to L_5) at a high water period (April 1, 2023) and at a low water period (July 1, 2023). The white mask indicates depths where the standard deviation, between the mean V_S model and all other accepted models during inversion, is greater than 400 m/s. Estimated GWT levels, obtained using DCs at seismic array points around PZ_3 (L_1-P_{22}, L_1-P_{23}, L_1-P_{24}, L_2-P_{21}, L_2-P_{22}, and L_2-P_{23}) and observed GWT levels at PZ_3 as training data, and geologic logs, illustrating the nature of the underground materials at five drilling coordinates, are superposed for interpretation.

across diverse geological settings is needed. By leveraging geophysical data and DL, the study contributes to advancing our understanding of subsurface dynamics and offers practical insights for effective GW management and risk mitigation strategies. This integrated approach can be applied to monitor aquifer resilience at different scales, contribute to informed decision-making in the context of water resource management, and assess potential hazards such as sinkholes.

Open Research Section

All authors approved the final version of this article. Input data files and Python scripts used for the GWT level estimations are available on the online Zenodo repository (`https://doi.org/10.5281/zenodo.10854339`) and on the GitHub repository (`https://github.com/JoseCunhaTeixeira/GWT_prediction`).

Acknowledgments

This research was made possible through funding from SNCF Réseau, CNRS, Sorbonne Université, Mines Paris-PSL research contract, and the ANRT/Cifre-SNCF Réseau n°2021/1552 convention. It is essential to acknowledge the contribution of the team involved in acquiring and processing the geophysical passive-MASW data. The successful execution of this study owes much to the efforts of the SERCEL Company, and particularly to the dedicated individuals Thomas Bardainne, Renaud Tarnus, Nicolas Deladerriere, Ceifang Cai, Loic Michel, Lilas Vivin, and Helene Toubiana Lille. The authors also express gratitude to the local teams from SNCF Réseau their invaluable assistance and support, notably to Fabrice Pierron for all the GIS cartography. The deep learning model was coded using Python package *Keras* (Chollet et al., 2015). Dispersion curve inversions were conducted using the open-source software package *SWIP*[1] implemented by Pasquet and Bodet (2017).

[1] `https://github.com/spasquet/SWIP`

Appendix A Raw data

Figure A1 shows the same V_R pseudo-sections presented in Figure 2, at a high water period on April 1, 2023, and at a low water period on July 1, 2023, but with DCs sampled over frequencies ranging from 5 to 50 Hz.

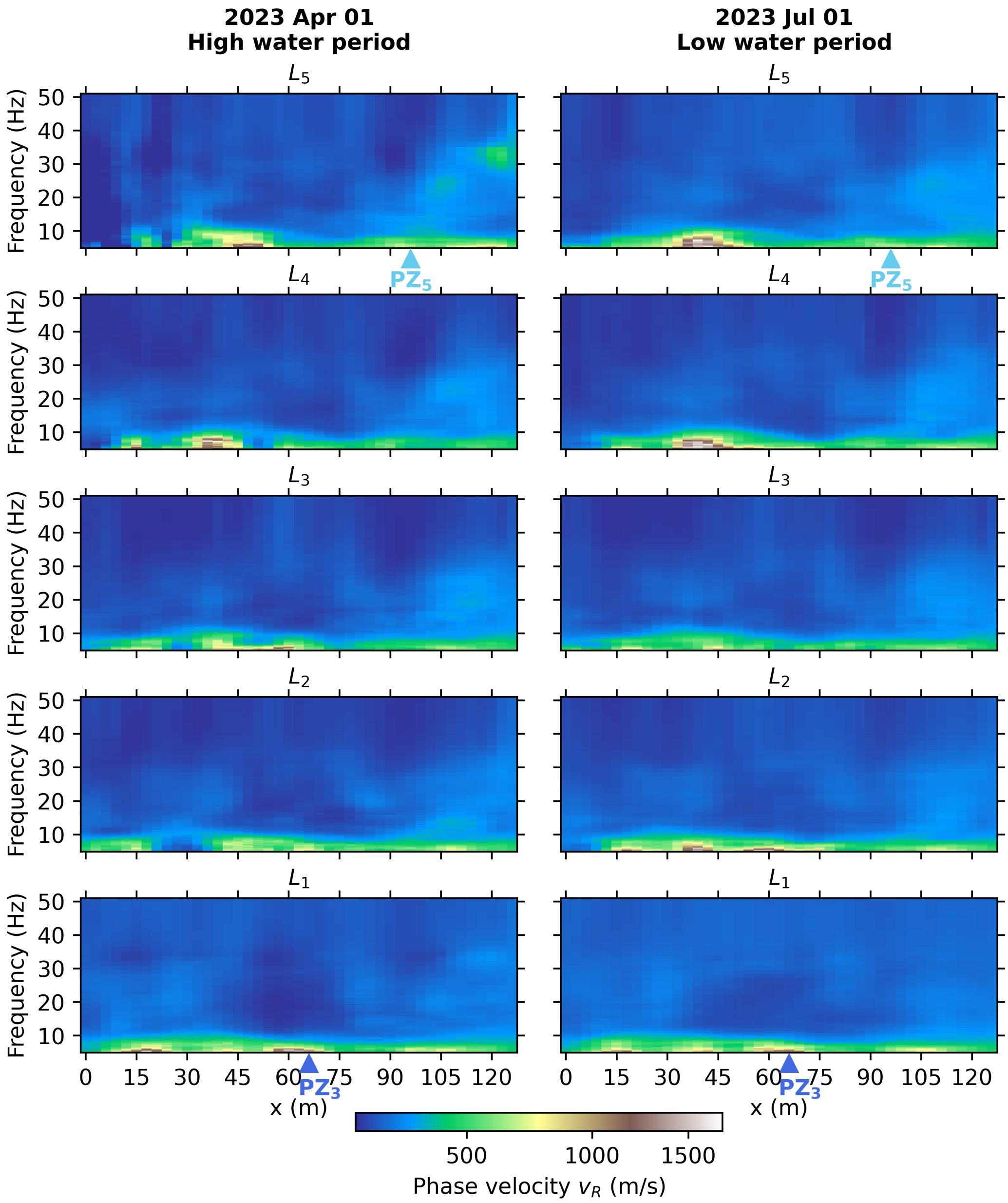

Figure A1. V_R pseudo-sections over frequencies for the 5 linear geophone arrays (L_1 to L_5) (left) at a high water period on April 1, 2023, and (right) at a low water period on July 1, 2023. Positions of piezometers PZ_3 and PZ_5 are represented by the blue triangles on profiles L_1 and L_5, respectively.

Appendix B Model trained with both piezometers

In this section, we present the same study, but incorporating results from a MLP model trained using seismic and GWT level data from both piezometers. The expanded dataset enhances the model's training with a more comprehensive understanding of the subsurface dynamics at multiple locations. By integrating seismic and GWT data from both piezometers, we aim to provide a more robust and nuanced analysis of the GWT variations and their correlation with the subsurface characteristics. Results are similar to those obtained using a single piezometer for training, and are discussed in Section 5.

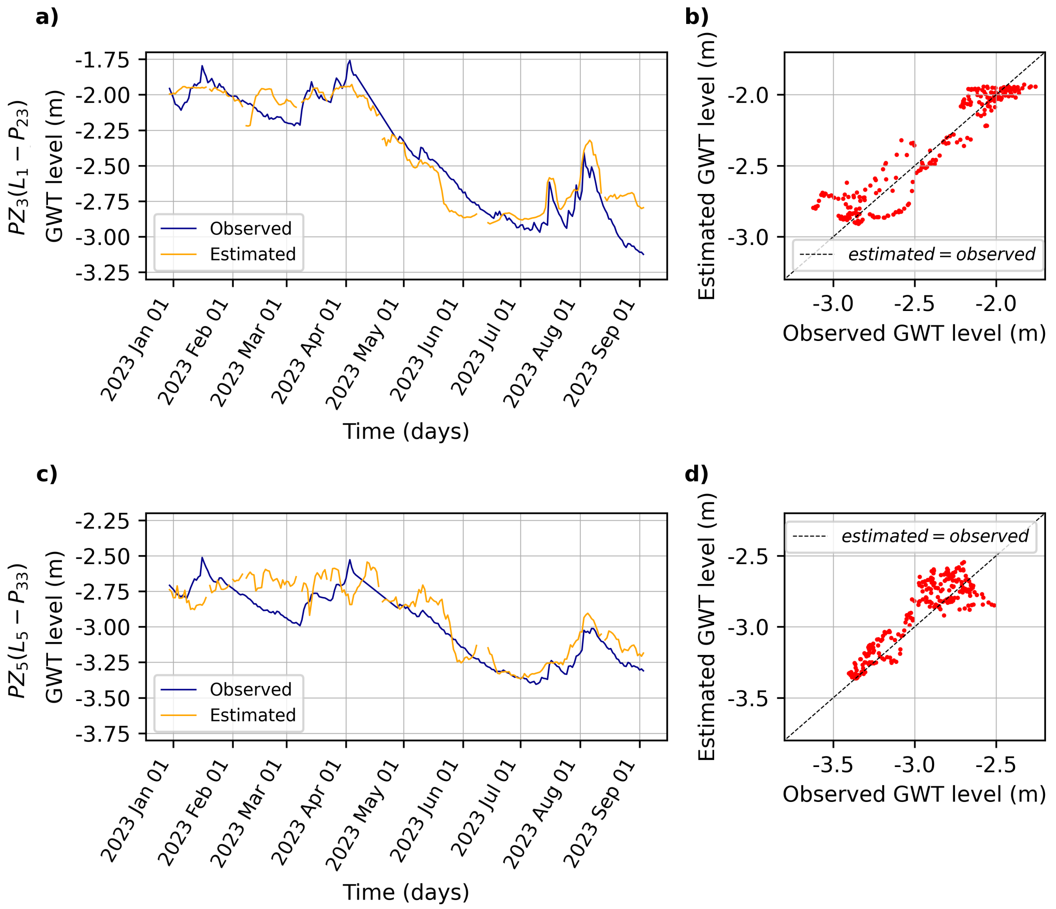

Figure B1. MLP's GWT level estimations, obtained using DCs at seismic array points around PZ_3 (L_1-P_{22}, L_1-P_{23}, L_1-P_{24}, L_2-P_{21}, L_2-P_{22}, and L_2-P_{23}) and PZ_5 (L_4-P_{31}, L_4-P_{32}, L_4-P_{33}, L_5-P_{32}, L_5-P_{33}, and L_5-P_{34}), and observed GWT levels at PZ_3 and PZ_5 as training data. (a) GWT level over time observed at PZ_3 and estimated at seismic array point L_1-P_{23}. (b) GWT levels observed at PZ_3 versus estimated at L_1-P_{23}. (c) GWT level over time observed at PZ_5 and estimated at seismic array point L_5-P_{33}. (d) GWT levels observed at PZ_5 versus estimated at point L_5-P_{33}.

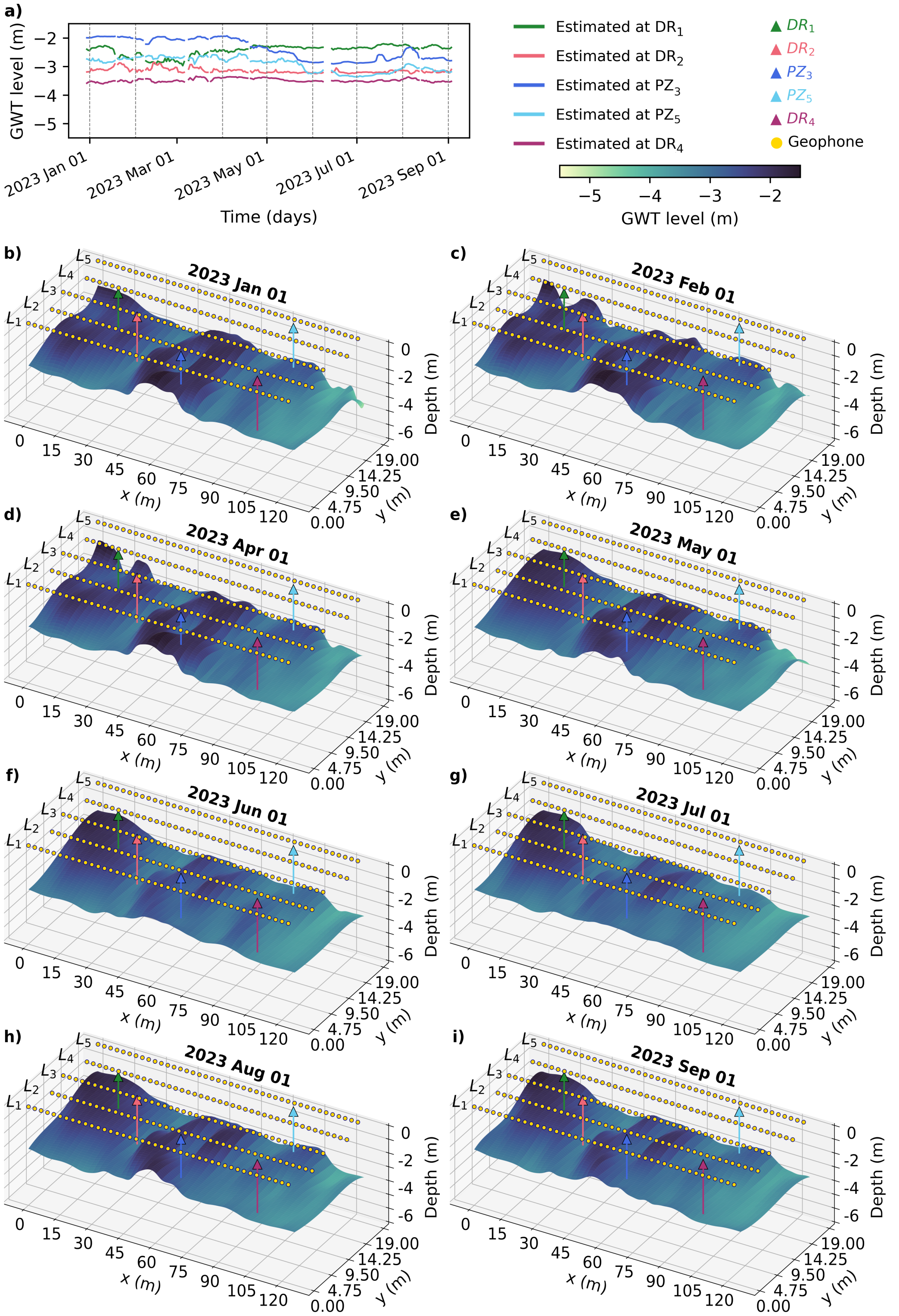

Figure B2. MLP's GWT level estimations, obtained using DCs at seismic array points around PZ_3 (L_1-P_{22}, L_1-P_{23}, L_1-P_{24}, L_2-P_{21}, L_2-P_{22}, and L_2-P_{23}) and PZ_5 (L_4-P_{31}, L_4-P_{32}, L_4-P_{33}, L_5-P_{32}, L_5-P_{33}, and L_5-P_{34}), and observed GWT levels at PZ_3 and PZ_5 as training data. (a) Estimated GWT levels over time at the five drilling and piezometers locations. (b) to (i) Estimated GWT level 2D maps at different dates, with geophone linear array ($L_{\#}$), piezometer ($PZ_{\#}$) and drilling ($DR_{\#}$) positions at the surface.

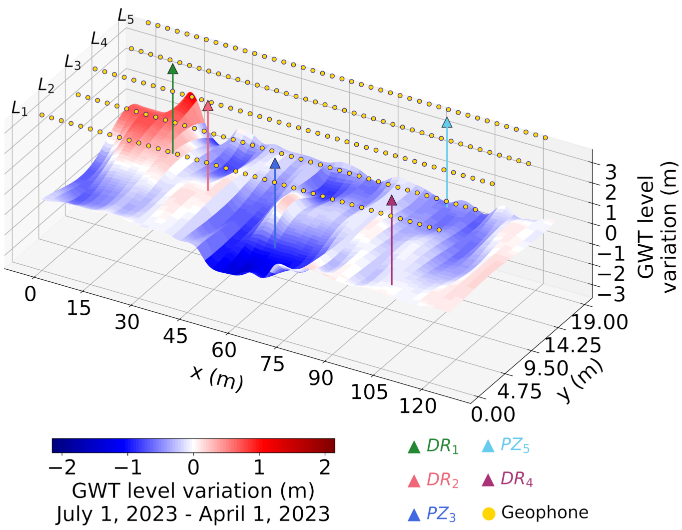

Figure B3. Estimated GWT level 2D map variation between high water period (April 1, 2023) and low water period (July 1, 2023), obtained using DCs at seismic array points around PZ_3 (L_1-P_{22}, L_1-P_{23}, L_1-P_{24}, L_2-P_{21}, L_2-P_{22}, and L_2-P_{23}) and PZ_5 (L_4-P_{31}, L_4-P_{32}, L_4-P_{33}, L_5-P_{32}, L_5-P_{33}, and L_5-P_{34}), and observed GWT levels at PZ_3 and PZ_5 as training data. Geophone, piezometer and drilling positions are displayed at surface.

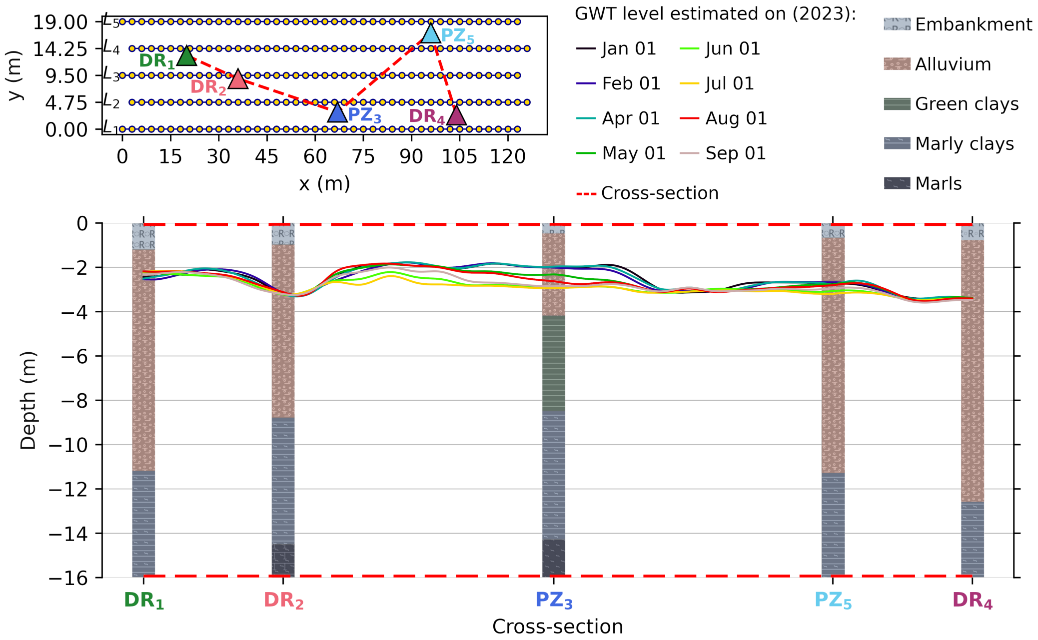

Figure B4. (a) Geophone array map and cross-section line (in red) between drilling and piezometers. (b) Cross-section of estimated GWT levels at different dates, obtained using DCs at seismic array points around PZ_3 (L_1-P_{22}, L_1-P_{23}, L_1-P_{24}, L_2-P_{21}, L_2-P_{22}, and L_2-P_{23}) and PZ_5 (L_4-P_{31}, L_4-P_{32}, L_4-P_{33}, L_5-P_{32}, L_5-P_{33}, and L_5-P_{34}), and observed GWT levels at PZ_3 and PZ_5 as training data, with geologic logs illustrating the nature of the underground materials.

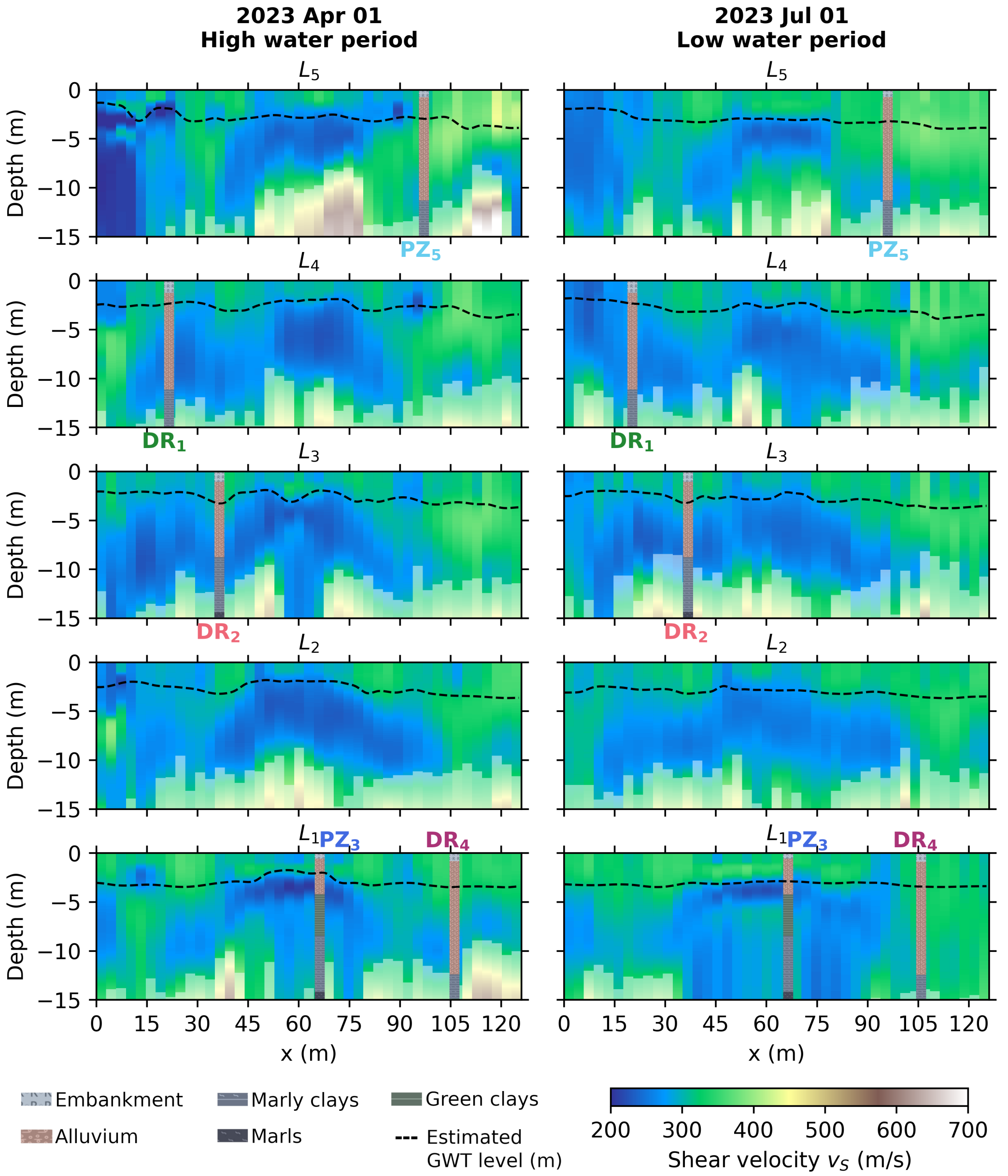

Figure B5. Inverted V_S sections over depth for the 5 linear geophone arrays (L_1 to L_5) at a high water period (April 1, 2023) and at a low water period (July 1, 2023). The white mask indicates depths where the standard deviation, between the mean V_S model and all other accepted models during inversion, is greater than 400 m/s. Estimated GWT levels, obtained using DCs at seismic array points around PZ_3 (L_1-P_{22}, L_1-P_{23}, L_1-P_{24}, L_2-P_{21}, L_2-P_{22}, and L_2-P_{23}) and PZ_5 (L_4-P_{31}, L_4-P_{32}, L_4-P_{33}, L_5-P_{32}, L_5-P_{33}, and L_5-P_{34}), and observed GWT levels at PZ_3 and PZ_5 as training data., and geologic logs, illustrating the nature of the underground materials at five drilling coordinates, are superposed for interpretation.

Appendix C Inversion

For each seismic linear array, V_R over frequencies pseudo-section, corresponding to DCs along x (fundamental mode M_0), obtained by passive-MASW, were inverted to generate a V_S over depth sections. We use the open-source software package *SWIP*[2] implemented by Pasquet and Bodet (2017), that is built upon the software *Dinver*[3] that uses a *neighbourhood algorithm* developed by (Sambridge, 1999) and implemented by (Wathelet, 2008), to solve the inverse problem in a juxtaposed 1D setup. The inversion was parameterized with five layers, including an half-space, in accordance with the drilling data (see PZ_3 in Figure 1). This method involves a stochastic exploration of a parameter space in order to search for a minimum misfit between measured and simulated DCs. The chosen parameter space, as outlined in Table C1, encompasses various key parameters including layer thicknesses, pressure-wave velocity (V_P), shear-wave velocity (V_S), density (ρ), and Poisson's ratio (ν). The deliberate selection of a large parameter space stems from the limited *a priori* information about the mechanical properties of the geological layers. This approach ensures that the inversion process remains explorative, unbiased, and is capable of capturing a wide range of geological scenarios that may influence the seismic response in the study area. For each DC along the seismic linear arrays, out of a total 200,400 simulated models, only the models with DCs within the error-bars are accepted and averaged to generate final average smooth velocity models. The running parameters using in *SWIP* are outlined in Table C2.

As examples, we present the inversion results at PZ_3 and PZ_5 positions on April 1, 2023, and July 1, 2023. Figure C1 shows the velocity models and corresponding DCs simulated during the inversion on April 1, 2023, and July 1, 2023, respectively. Each DC and velocity model is represented with a color depending on the misfit value (MF) between the experimental data (black crosses and error-bars) and the simulated dispersion defined as:

$$MF = \sqrt{\sum_{i=1}^{N_f} \frac{(V_{sim_i} - V_{exp_i})^2}{N_f \sigma_i^2}} \ , \tag{C1}$$

[2] `https://github.com/spasquet/SWIP`

[3] `https://www.geopsy.org/wiki/index.php/Dinver:_dinverdc`

with V_{sim_i} and V_{exp_i} being the simulated and experimental phase velocities at each frequency f_i, N_f the number of frequency samples, and σ_i the phase-velocity measurement uncertainty (error-bars) at each frequency f_i.

Table C1. Inversion parameter space.

Layer (#)	Thickness (m)	V_P (m/s)	V_S (m/s)	ρ (kg/m^3)	ν
1	1-10	100-1000	50-500	2000-2500	0.1-0.5
2	1-10	100-1000	50-500	2000-2500	0.1-0.5
3	1-10	100-1000	50-500	2000-2500	0.1-0.5
4	1-20	200-2000	100-1000	2000-2500	0.1-0.5
$\frac{1}{2}$-space	∞	400-4000	200-2000	2000-2500	0.1-0.5

Table C2. Inversion running parameters in *SWIP*.

Parameter	Value	Description
n_{run}	4	Number of runs
it_{max}	250	Number of iterations per run
ns_0	100	Number of starting models
ns	200	Number of modes created at each iteration
nr	100	Number of previous models to build new sub-parameter space

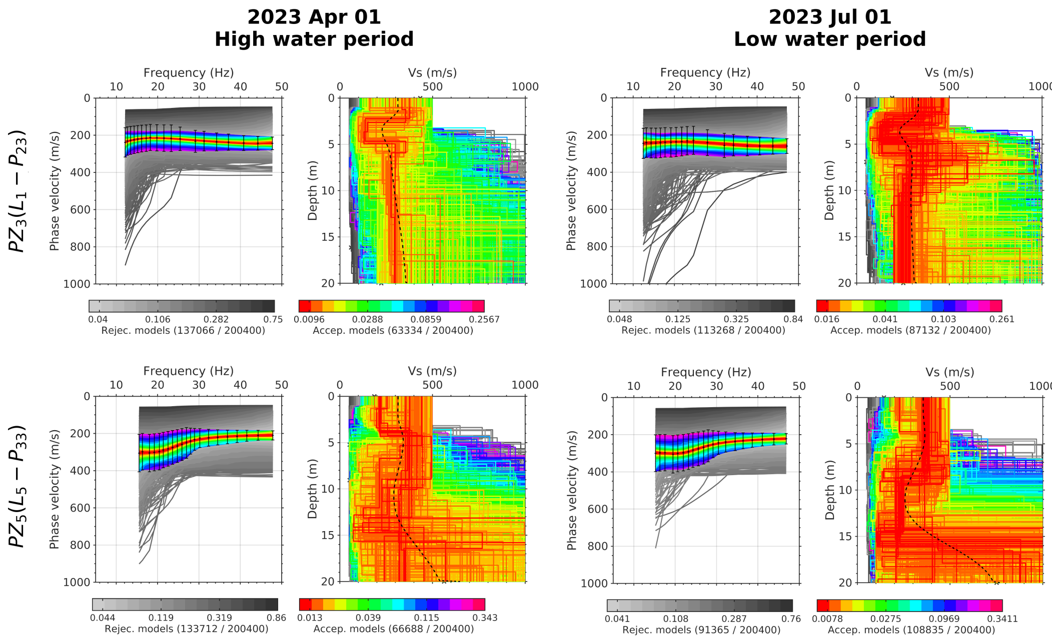

Figure C1. Inversion results at seismic array points (top) L_1-P_{23}, close to $PZ3$, and (bottom) L_5-P_{33}, close to $PZ5$, on (left) on April 1, 2023, and July 1, 2023. (a), (c), (e), and (g) show the modeled DCs, with error-bars, for the fundamental mode. (b), (d), (f), and (h) represent the modeled velocity models. Each DC and velocity model is represented with a color depending on the misfit value between the modeled and experimental DCs (black crosses and error-bars). The models inside the error-bars, in terms of DCs, are plotted in color, and the rest are plotted in a gray scale. Plotted from the inversion software *SWIP*.

Appendix D Error computation

The *root mean squared error* (RMSE) corresponds to the expected value of the squared error or loss. If $\hat{y}_i$ is the predicted value of the i-th samples, and y_i is the corresponding true value, then the RMSE estimated over $n_{samples}$ is defined as :

$$RMSE(y, \hat{y}) = \frac{1}{n_{samples}} \sum_{i=1}^{n_{samples}} (y_i - \hat{y}_i)^2 \ . \tag{D1}$$

The coefficient of determination, usually denoted R^2, represents the proportion of variance that has been explained by the independent variables in the model. It provides an indication of goodness of fit and therefore a measure of how well unseen samples are likely to be predicted by the model, through the proportion of explained variance. If $\hat{y}_i$ is the predicted value of the i-th samples, and y_i is the corresponding true value, then the R^2 score over $n_{samples}$ is defined as :

$$R^2(y, \hat{y}) = 1 - \frac{\sum_{i=1}^{n_{samples}} (y_i - \hat{y}_i)^2}{\sum_{i=1}^{n_{samples}} (y_i - \tilde{y}_i)^2} \ , \tag{D2}$$

where $\tilde{y} = \frac{1}{n_{samples}} \sum_{i=1}^{n_{samples}} y_i$ is the arithmetic mean value of y.

References

Abi Nader, A., Albaric, J., Steinmann, M., Hibert, C., Malet, J.-P., Sue, C., … Boetsch, A. (2023). Machine learning prediction of groundwater heights from passive seismic wavefield. *Geophysical Journal International*, *234*(3), 1807-1818. doi: 10.1093/gji/ggad160

Aki, K. (1957). Space and time spectra of stationary stochastic waves, with special reference to microtremors. *Bulletin of the Earthquake Research Institute*, *35*, 415–456.

Barajas, A., Poli, P., D'Agostino, N., Margerin, L., & Campillo, M. (2021). Separation of poroelastic and elastic processes of an aquifer from tectonic phenomena using geodetic, seismic, and meteorological data in the pollino region, italy. *Geochemistry, Geophysics, Geosystems*, *22*(11), e2021GC009742. doi: 10.1029/2021GC009742

Bardaine, T., & Rondeleux, B. (2018). *Method and device for monitoring the subsoil of the earth under a target zone* (patent No. FR3084473B1). Retrieved from `https://patents.google.com/patent/WO2020021177A1/en?inventor=Bardainne&oq=Bardainne`

Bardainne, T., Tarnus, R., Deladerriere, N., Hallier, A., Boisson-Gaboriau, J., Valentin, J., … Bouhdiche, O. (2022). Permanent passive seismic monitoring of the near-surface ground beneath railways using trains as sources. In (Vol. 1, p. 14). Fifth International Conference on Railway Technology: Research, Development and Maintenance.

Bardainne, T., Vivin, L., & Tarnus, R. (2023). Railway near-surface passive seismic using trains as sources and fiber optic monitoring. In (Vol. 2023, p. 1–5). European Association of Geoscientists & Engineers. doi: 10.3997/2214-4609.202320093

Bergamo, P., Dashwood, B., Uhlemann, S., Swift, R., Chambers, J., Gunn, D., & Donohue, S. (2016). Time-lapse monitoring of climate effects on earthworks using surface waves. *Geophysics*, *81*, EN1-EN15. doi: 10.1190/GEO2015-0275.1

Biot, M. A. (1956a). Theory of Propagation of Elastic Waves in a Fluid-Saturated Porous Solid. I. Low-Frequency Range. *The Journal of the Acoustical Society of America*, *28*(2), 168-178. doi: 10.1121/1.1908239

Biot, M. A. (1956b). Theory of Propagation of Elastic Waves in a Fluid-Saturated Porous Solid. II. Higher Frequency Range. *The Journal of the Acoustical Society of America*, *28*(2), 179-191. doi: 10.1121/1.1908241

Cai, H., Liu, S., Shi, H., Zhou, Z., Jiang, S., & Babovic, V. (2022). Toward improved lumped groundwater level predictions at catchment scale: Mutual integration of water balance mechanism and deep learning method. *Journal of Hydrology*, *613*, 128495. doi: https://doi.org/10.1016/j.jhydrol.2022.128495

Cheng, F., Xia, J., Luo, Y., Xu, Z., Wang, L., Shen, C., ... Hu, Y. (2016). Multichannel analysis of passive surface waves based on crosscorrelations. *Geophysics*, *81*(5), EN57–EN66. doi: 10.1190/geo2015-0505.1

Cheng, F., Xia, J., Xu, Y., Xu, Z., & Pan, Y. (2015). A new passive seismic method based on seismic interferometry and multichannel analysis of surface waves. *Journal of Applied Geophysics*, *117*. doi: 10.1016/j.jappgeo.2015.04.005

Chollet, F., et al. (2015). *Keras.* `https://keras.io`.

Clements, T., & Denolle, M. A. (2018). Tracking groundwater levels using the ambient seismic field. *Geophysical Research Letters*, *45*(13), 6459-6465. doi: 10.1029/2018GL077706

Cunha Teixeira, J., Bodet, L., Dangeard, M., Gesret, A., Hallier, A., Rivière, A., ... Boisson Gaboriau, J. (submitted). Passive measurement of multi-modal surface-wave dispersion along high-speed lines using uniform linear arrays. *Seismica*.

Czarny, R., Zhu, T., & Shen, J. (2023). Spatiotemporal evaluation of rayleigh surface wave estimated from roadside dark fiber das array and traffic noise. *Seismica*, *2*(22). doi: 10.26443/seismica.v2i2.247

Dafflon, B., Irving, J., & Holliger, K. (2009). Use of high-resolution geophysical data to characterize heterogeneous aquifers: Influence of data integration method on hydrological predictions. *Water Resources Research*, *45*(9). doi: 10.1029/2008WR007646

Dagan, G. (1982). Stochastic modeling of groundwater flow by unconditional and conditional probabilities: 1. conditional simulation and the direct problem. *Water Resources Research*, *18*(4), 813-833. doi: 10.1029/WR018i004p00813

Dangeard, M., Rivière, A., Bodet, L., Schneider, S., Guérin, R., Jougnot, D., & Maineult, A. (2021). River corridor model constrained by time-lapse seismic acquisition. *Water Resources Research*, *57*(10), e2020WR028911. doi: 10.1029/2020WR028911

Derode, A., Larose, E., Tanter, M., de Rosny, J., Tourin, A., Campillo, M., & Fink, M. (2003). Recovering the green's function from field-field correlations in an open scattering medium (l). *The Journal of the Acoustical Society of America*, *113*(6), 2973–2976. doi: 10.1121/1.1570436

Foti, S., Hollender, F., Garofalo, F., Albarello, D., Asten, M., Bard, P.-Y., ... Socco, L. V. (2018). Guidelines for the good practice of surface wave analysis: a product of the interpacific project. *Bulletin of Earthquake Engineering*, *16*. doi: 10.1007/s10518-017-0206-7

Garambois, S., Sénéchal, P., & Perroud, H. (2002). On the use of combined geophysical methods to assess water content and water conductivity of near-surface formations. *Journal of Hydrology*, *259*, 32-48. doi: 10.1016/s0022-1694(01)00588-1

Garambois, S., Voisin, C., Romero Guzman, M. A., Brito, D., Guillier, B., & Réfloch, A. (2019). Analysis of ballistic waves in seismic noise monitoring of water table variations in a water field site: added value from numerical modelling to data understanding. *Geophysical Journal International*, *219*(3), 1636-1647. doi: 10.1093/gji/ggz391

Gaubert-Bastide, T., Garambois, S., Bordes, C., Voisin, C., Oxarango, L., Brito, D., & Roux, P. (2022). High-resolution monitoring of controlled water table variations from dense seismic-noise acquisitions. *Water Resources Research*, *58*(8), e2021WR030680. doi: 10.1029/2021WR030680

Grêt, A., Snieder, R., & Scales, J. (2006). Time-lapse monitoring of rock properties with coda wave interferometry. *Journal of Geophysical Research: Solid Earth*, *111*(B3). doi: 10.1029/2004JB003354

Gutiérrez, F., Parise, M., De Waele, J., & Jourde, H. (2014). A review on natural and human-induced geohazards and impacts in karst. *Earth-Science Reviews*, *138*, 61–88. doi: 10.1016/j.earscirev.2014.08.002

Hermans, T., Goderniaux, P., Jougnot, D., Fleckenstein, J. H., Brunner, P., Nguyen, F., ... Le Borgne, T. (2023). Advancing measurements and representations of subsurface heterogeneity and dynamic processes: towards 4d hydrogeology. *Hydrology and Earth System Sciences*, *27*(1), 255–287. doi: 10.5194/hess-27-255-2023

Jougnot, D., Linde, N., Haarder, E., & Looms, M. (2015). Monitoring of saline tracer movement with vertically distributed self-potential measurements at the hobe agricultural site, voulund, denmark. *Journal of Hydrology*, *521*, 314-327. doi: 10.1016/j.jhydrol.2014.11.041

Kim, D., & Lekic, V. (2019). Groundwater variations from autocorrelation and receiver functions. *Geophysical Research Letters*, *46*(23), 13722-13729. doi: 10.1029/2019GL084719

Kingma, D., & Ba, J. (2014). Adam: A method for stochastic optimization. *International Conference on Learning Representations*.

Kleinhans, M. G. (2005). Flow discharge and sediment transport models for estimating a minimum timescale of hydrological activity and channel and delta formation on mars. *Journal of Geophysical Research: Planets*, *110*(E12). doi: 10.1029/2005JE002521

Klotzsche, A., Jonard, F., Looms, M., van der Kruk, J., & Huisman, J. (2018). Measuring soil water content with ground penetrating radar: A decade of progress. *Vadose Zone Journal*, *17*(1), 180052. doi: 10.2136/vzj2018.03.0052

Larose, E., Carrière, S., Voisin, C., Bottelin, P., Baillet, L., Guéguen, P., ... Massey, C. (2015). Environmental seismology: What can we learn on earth surface processes with ambient noise? *Journal of Applied Geophysics*, *116*, 62–74. doi: 10.1016/j.jappgeo.2015.02.001

Lecocq, T., Longuevergne, L., Pedersen, H., Brenguier, F., & Stammler, K. (2017). Monitoring ground water storage at mesoscale using seismic noise: 30 years of continuous observation and thermo-elastic and hydrological modeling. *Scientific Reports*, *7*. doi: 10.1038/s41598-017-14468-9

Linnainmaa, S. (1976). Taylor expansion of the accumulated rounding error. *BIT Numerical Mathematics*, *16*(2), 146–160. doi: 10.1007/BF01931367

Loeffler, O. H., & Bano, M. (2004). Ground penetrating radar measurements in a controlled vadose zone: influence of the water content. *Vadose Zone Journal*, *3*, 1082-1092. doi: 10.2113/3.4.1082

Lu, Z. (2014). Feasibility of using a seismic surface wave method to study seasonal and weather effects on shallow surface soils. *Journal of Environmental & Engineering Geophysics*, *19*, 71-85. doi: 10.2113/JEEG19.2.71

Maillot, M., Flipo, N., Rivière, A., Desassis, N., Renard, D., Goblet, P., & Vincent, M. (2019). Technical note: Water table mapping accounting for river–aquifer connectivity and human pressure. *Hydrology and Earth System Sciences*, *23*(11), 4835–4849. doi: 10.5194/hess-23-4835-2019

Mao, S., Lecointre, A., van der Hilst, R., & Campillo, M. (2022). Space-time monitoring of groundwater fluctuations with passive seismic interferometry. *Nature Communications*, *13*, 4643. doi: 10.1038/s41467-022-32194-3

Mi, B., Xia, J., Tian, G., Shi, Z., Xing, H., Chang, X., ... Zhang, H. (2022). Near-surface imaging from traffic-induced surface waves with dense linear arrays: An application in the urban area of hangzhou, china. *Geophysics*, *87*(2), B145–B158. doi: 10.1190/geo2021-0184.1

Mi, B., Xia, J., Xu, Y., You, B., & Chen, Y. (2023). Retrieval of surface waves from high-speed-train-induced vibrations using seismic interferometry. *Geophysics.*. doi: 10.1190/geo2022-0603.1

Murtagh, F. (1991). Multilayer perceptrons for classification and regression. *Neurocomputing*, *2*(5), 183-197. doi: 10.1016/0925-2312(91)90023-5

Nguyen-Thé, D., Ollagnier, S., Pétrignet, M., Thonnon, J., & Joannes, O. (2010). *Carte piézométrique de la nappe des grès du Trias inférieur de 2010. Report BRGM/RP-59294-FR.*

Panda, S., Kumar, S., Pradhan, S., Sidhu, J., Kralia, A., & Thakur, D. M. (2022). Effect of groundwater table fluctuation on slope instability: a comprehensive 3d simulation approach for kotropi landslide, india. *Landslides*. doi: 10.1007/s10346-022-01993-6

Parise, M. (2019). Sinkholes. In W. B. White, D. C. Culver, & T. Pipan (Eds.), *Encyclopedia of caves (third edition)* (Third ed., p. 934-942). Academic Press. doi: 10.1016/B978-0-12-814124-3.00110-2

Park, C. B., & Miller, R. D. (2008). Roadside Passive Multichannel Analysis of Surface Waves (MASW). *Journal of Environmental and Engineering Geophysics*, *13*(1), 1–11. doi: 10.2113/JEEG13.1.1

Park, C. B., Miller, R. D., & Xia, J. (1999). Multichannel analysis of surface waves. *Geophysics*, *64*(3), 800–808. doi: 10.1190/1.1444590

Pasquet, S., & Bodet, L. (2017). Swip: An integrated workflow for surface-wave dispersion inversion and profiling. *Geophysics*, *82*(6), WB47–WB61. doi: 10.1190/geo2016-0625.1

Pasquet, S., Bodet, L., Dhemaied, A., Mouhri, A., Vitale, Q., Rejiba, F., … Guérin, R. (2015a). Detecting different water table levels in a shallow aquifer with combined p-, surface and sh-wave surveys: Insights from vp/vs or poisson's ratios. *Journal of Applied Geophysics*, *113*. doi: 10.1016/j.jappgeo.2014.12.005

Pasquet, S., Bodet, L., Longuevergne, L., Dhemaied, A., Camerlynck, C., Rejiba, F., & Guérin, R. (2015b). 2d characterization of near-surface vp/vs: Surface-wave dispersion inversion versus refraction tomography. *Near Surface Geophysics*, *13*. doi: 10.3997/1873-0604.2015028

Qin, L., Steidl, J. H., Qiu, H., Nakata, N., & Ben-Zion, Y. (2022). Monitoring seasonal shear wave velocity changes in the top 6 m at garner valley in southern california with borehole data. *Geophysical Research Letters*, *49*(23), e2022GL101189. doi: 10.1029/2022GL101189

Quiros, D. A., Brown, L. D., & Kim, D. (2016). Seismic interferometry of railroad induced ground motions: body and surface wave imaging. *Geophysical Journal International*, *205*(1), 301-313. doi: 10.1093/gji/ggw033

Rahardjo, H., Satyanaga, A., Leong, E., & Ng, Y. (2010). Effects of groundwater table position and soil properties on stability of slope during rainfall. *Journal of Geotechnical and Geoenvironmental Engineering*, *136*, 1555–1564. doi: 10.1061/(ASCE)GT.1943-5606.0000385

Rezaeifar, M., Lavoué, F., Maggio, G., Xu, Y., Bean, C. J., Pinzon-Rincon, L., … Brenguier, F. (2023). Imaging shallow structures using interferometry of seismic body waves generated by train traffic. *Geophysical Journal International*, *233*(2), 964–977. doi: 10.1093/gji/ggac507

Rosenblatt, F. (1958). The perceptron: A probabilistic model for information storage and organization in the brain. *Psychological Review*, *65*(6), 386–408. doi: 10.1037/h0042519

Sambridge, M. (1999). Geophysical inversion with a neighbourhood algorithm—i. searching a parameter space. *Geophysical Journal International*, *138*(2), 479–494. doi: 10.1046/j.1365-246X.1999.00876.x

Samouëlian, A., Cousin, I., Tabbagh, A., Bruand, A., & Richard, G. (2005). Electrical resistivity survey in soil science: a review. *Soil and Tillage Research*, *83*(2), 173-193. doi: 10.1016/j.still.2004.10.004

Sanchez Gonzalez, R., Bodet, L., Gesret, A., & Rivière, A. (in prep). Bayesian estimation of van Genuchten parameters in unsaturated and unconsolidated soils using seismic data. *Geophysical Journal International*.

Shorten, C., & Khoshgoftaar, T. M. (2019). A survey on image data augmentation for deep learning. *Journal of Big Data*, *6*(1), 60. doi: 10.1186/s40537-019-0197-0

Shtivelman, V. (1999). Using surface waves for estimating shear wave velocities in the shallow subsurface onshore and offshore israel. *European Journal of Environmental and Engineering Geophysics*, *4*, 15-35.

Solazzi, S. G., Bodet, L., Holliger, K., & Jougnot, D. (2021). Surface-wave dispersion in partially saturated soils: The role of capillary forces. *Journal of Geophysical Research: Solid Earth*, *126*(12), e2021JB022074. doi: 10.1029/2021JB022074

Tarnus, R., Bardainne, T., Michel, L., Deladerriere, N., & Cai, C. (2022a). A case study for railway underground imaging using trains as seismic signal for sinkhole and subsidence phenomena prevention. In (Vol. 1, p. 13). Fifth International Conference on Railway Technology: Research, Development and Maintenance.

Tarnus, R., Bardainne, T., Michel, L., Deladerriere, N., Cai, C., Hallier, A., & Boisson-Gaboriau, J. (2022b). A case study for underground imaging using trains as seismic signal to investigate subsidence phenomena. In (Vol. 2022, p. 1–5). European Association of Geoscientists & Engineers. doi: 10.3997/2214-4609.202220033

Tripathy, K., & Mishra, A. (2024). Deep learning in hydrology and water resources disciplines: Concepts, methods, applications, and research directions. *Journal of Hydrology*, *628*, 130458. doi: 10.1016/j.jhydrol.2023.130458

Tsai, F. T.-C., & Li, X. (2008). Inverse groundwater modeling for hydraulic conductivity estimation using bayesian model averaging and variance window. *Water Resources Research*, *44*(9). doi: 10.1029/2007WR006576

Voisin, C., Garambois, S., Massey, C., & Brossier, R. (2016). Seismic noise monitoring of the water table in a deep-seated, slow-moving landslide. *Interpretation*, *4*(3), SJ67-SJ76. doi: 10.1190/INT-2016-0010.1

Voisin, C., Guzmán, M., Réfloch, A., Taruselli, M., & Garambois, S. (2017). Groundwater monitoring with passive seismic interferometry. *Journal of Water Resource and Protection*, *9*, 1414-1427. doi: 0.4236/jwarp.2017.912091

Waltham, T., Bell, F., & Culshaw, M. (2004). *Sinkholes and subsidence: karst and cavernous rocks in engineering and construction* (2005th ed.). Springer. doi: 10.1007/b138363

Wapenaar, K. (2004). Retrieving the elastodynamic green's function of an arbitrary inhomogeneous medium by cross correlation. *Physical Review Letters*, *93*(25), 254301. doi: 10.1103/PhysRevLett.93.254301

Wapenaar, K., Draganov, D., Snieder, R., Campman, X., & Verdel, A. (2010a). Tutorial on seismic interferometry. part i: Basic principles and applications. *Geophysics*, *75*, 75A195-75209. doi: 10.1190/1.3457445

Wapenaar, K., Slob, E., Snieder, R., & Curtis, A. (2010b). Tutorial on seismic interferometry: Part 2 — underlying theory and new advances. *Geophysics*, *75*, 75A211-75227. doi: 10.1190/1.3463440

Wathelet, M. (2008). An improved neighborhood algorithm: Parameter conditions and dynamic scaling. *Geophysical Research Letters*, *35*(9). doi: 10.1029/2008GL033256

Weaver, R. L., & Lobkis, O. I. (2004). Diffuse fields in open systems and the emergence of the green's function (l). *The Journal of the Acoustical Society of America*, *116*(5), 2731–2734. doi: 10.1121/1.1810232

Werbos, P. J. (1982). Applications of advances in nonlinear sensitivity analysis. In R. F. Drenick & F. Kozin (Eds.), *System modeling and optimization* (pp. 762–770). Berlin, Heidelberg: Springer Berlin Heidelberg.

Xiao, X., Gutiérrez, F., & Guerrero, J. (2020). The impact of groundwater drawdown and vacuum pressure on sinkhole development. physical laboratory models. *Engineering Geology*, *279*, 105894. doi: 10.1016/j.enggeo.2020.105894

Ying, X. (2019). An overview of overfitting and its solutions. *Journal of Physics: Conference Series*, *1168*, 022022. doi: 10.1088/1742-6596/1168/2/022022

You, B., Mi, B., Guan, B., Zhang, H., & Liu, Y. (2023). High-quality surface wave retrieval from vibrations generated by high-speed trains moving on viaducts. *Journal of Applied Geophysics*, *212*, 105005. doi: 10.1016/j.jappgeo.2023.105005

Zhang, S., Luo, B., Ben-Zion, Y., Lumley, D. E., & Zhu, H. (2023). Monitoring terrestrial water storage, drought and seasonal changes in central oklahoma with ambient seismic noise. *Geophysical Research Letters*, *50*(17), e2023GL103419. doi: 10.1029/2023GL103419